

Material data identification in generalized continua

Jacinto Ulloa^{a,*}, Laurent Stainier^b

^a*Department of Mechanical Engineering, University of Michigan, Ann Arbor, MI 48109, USA*

^b*Nantes Université, Ecole Centrale Nantes, CNRS, GeM, UMR 6183, F-44000 Nantes, France*

Abstract

We introduce a data-driven framework for identifying material behavior from full-field kinematics and force measurements in generalized (micromorphic) continua. Unlike traditional approaches that rely on constitutive assumptions or homogenization schemes, our method extracts generalized stress-strain data by enforcing non-classical balance laws and compatibility relations on full-field boundary value problems. Specifically, the approach infers the associated generalized stresses and constructs representative material datasets via clustering in a non-classical phase space. We show that the proposed method reliably extracts non-symmetric and higher-order local stress states, providing material data suitable for either model calibration or model-free data-driven simulations of generalized continua. These capabilities are demonstrated in validation simulations with synthetic data and in an application to mechanical metamaterials, suggesting a practical route for material characterization of microstructured solids.

Keywords: Data-driven computational mechanics, Material identification, Inverse problems, Generalized continua, Micromorphic continua

1. Introduction

Generalized continuum theories emerged from the need to describe material systems whose mechanical response is strongly influenced by internal microstructural effects, for which the physics supplied by classical Cauchy continuum theories is no longer sufficient [1]. Starting with the seminal work of the Cosserat brothers [2], which gave rise to the notion of micropolar continua, several decades of research have produced a broad family of generalized continuum formulations, including microstrain [3], gradient-enhanced [4], non-local [5], and micromorphic theories [6]. These theories capture complex phenomena related to microstructure [7–10], strain localization [4, 11–13], size effects [14–17], and wave dispersion [18–21] in a range of materials. Yet, despite substantial theoretical progress, the practical identification of constitutive relations for generalized continua remains a persistent challenge, particularly for complex micromorphic models, often rendering them elusive in applications. This limitation stems from the fact that generalized material states, in particular stress quantities, are inherently unmeasurable. Hence, the objective of the present work is to develop a model-free framework for identifying material stress-strain data directly from full-field kinematics and force measurements in generalized continua.

The cornerstone of Cosserat continua is the introduction of microrotational degrees of freedom and associated balance laws, giving rise to a continuum theory in which the classical symmetry of the stress tensor is relaxed. Non-symmetric stresses of this type arise from body and surface couples of mechanical origin or from other physical mechanisms, e.g., through the action of electromagnetic fields [22]. Although conceptually significant, the notion of generalized continua thus initiated remained dormant for

*Corresponding author

Email addresses: julloa@umich.edu (Jacinto Ulloa), laurent.stainier@ec-nantes.fr (Laurent Stainier)

several decades before being revived and substantially generalized in the 1960s and 1970s by Eringen and Suhubi [23], Eringen [24], Mindlin [25], and Germain [26]. These developments extended the Cosserat framework from rigid microrotations to fully deformable microstructures via generally non-symmetric microdeformation tensors and third-order stress measures, thereby establishing the class of micromorphic continua. The resulting theory is notably general, embedding several models as special cases (see Neff et al. [27] for a unified overview), including micropolar and second-gradient elasticity, and has since been adapted to describe, e.g., plasticity [28–32] and damage [33–36] (see Forest [37] for an overview in this context). Despite its unifying structure, practical applications of phenomenological micromorphic models face challenges in experimental identification and constitutive calibration due to the large number (and often unclear physical nature) of material parameters relating generalized strains to generalized stresses.

Pivoting away from traditional parameter-based constitutive models, model-free data-driven methods [38–42] circumvent the need for an explicit constitutive parameterization of material behavior. Rather than postulating phenomenological laws, these methods close the fundamental kinematic and balance equations with empirical data obtained directly from experiments or lower-scale simulations. While this approach is mostly developed for classical Cauchy continua, recent efforts have considered extensions to generalized continuum theories [43–45]. Nevertheless, much like constitutive models, generalized data-driven frameworks critically depend on the availability of generalized stress–strain data in the appropriate phase space, albeit intended for direct use in model-free simulations rather than parameter fitting.

Ideally, homogenization methods, based on either formal two-scale asymptotics or discrete-to-continuum variational analysis, would provide (i) an unambiguous effective continuum (energy) form and (ii) explicit effective material parameters. Such approaches are well established for linear Cauchy continua, and have also been developed for generalized continua arising from particular microstructures [7–9, 17, 46]. However, more generally, computational homogenization is employed, e.g., to derive generalized continuum quantities from heterogeneous but classical (Cauchy) materials defined at the scale of representative volume elements (RVEs). Developments in this context include homogenization towards micropolar [47–49], second-gradient [50–52], and micromorphic continua [10, 53–59]. More recently, Miller et al. [60] proposed a filter-based method that extracts micromorphic stresses and deformation measures via averaging rules in fully resolved direct numerical simulations. While these approaches demonstrate that generalized stress–strain data can, in principle, be extracted from microstructured materials, RVE-based homogenization schemes still depend critically on assumptions regarding the kinematic ansatz and higher-order boundary conditions at the unit-cell level. In turn, filter-based homogenization relies on microscale stresses and associated numerical averaging procedures. Consequently, no clear consensus currently exists on the computational characterization of effective generalized material states.

In light of these limitations, we propose to pivot away from homogenization altogether and instead extract generalized stress–strain data directly from full-field *kinematic* measurements and applied forces in boundary value problems (BVPs). Building upon previous developments for classical Cauchy materials [61, 62], the proposed framework is agnostic to the constitutive model and relies solely on enforcing non-classical balance laws and compatibility relations. In this way, it enables a direct identification of material data for generalized micromorphic continua, including non-symmetric and higher-order stresses. The identified data is then suitable for either material model calibration or model-free data-driven simulations.

The paper is structured as follows. Sections 2 and 3 provide a brief overview of micromorphic continuum mechanics and its data-driven reformulation, respectively. Section 4 presents the proposed data-driven identification method. Section 5 presents numerical validation simulations and an application to mechanical metamaterials, while section 6 concludes with a summary and outlook.

2. Overview of generalized micromorphic continua

2.1. Problem setting

Consider a *microstructured* deformable solid $\Omega \subset \mathbb{R}^n$ of spatial dimension n . The solid is described as a *generalized micromorphic continuum* [23, 25], such that, attached to each macro-coordinate $\mathbf{x} \in \Omega$, is a *micro-continuum* body Ω^m defined through micro-coordinates $\xi_i \in \Omega^m$ and subject to independent deformations (Figure 1). Then, the motion of a point (\mathbf{x}, ξ) is given by a *micro-displacement* field expressed as the sum of macro-displacement and fluctuation terms:

$$\mathbf{v}(\mathbf{x}, \xi) = \mathbf{u}(\mathbf{x}) + \boldsymbol{\chi}(\mathbf{x}) \cdot \xi + O(\|\xi\|^2), \quad \chi_{ij} = \frac{\partial v_i}{\partial \xi_j}. \quad (1)$$

The deformation process is thus characterized by a macro-displacement field $\mathbf{u} : \Omega \rightarrow \mathbb{R}^n$ and a micro-deformation field $\boldsymbol{\chi} : \Omega \rightarrow \mathbb{R}^{n \times n}$. When the latter is presumed homogeneous in Ω^m , i.e., independent of $\xi \in \Omega^m$, we recover a micromorphic theory of degree one [26].

The macroscopic BVP is then given in terms of the primary fields \mathbf{u} and $\boldsymbol{\chi}$, the latter representing an additional set of degrees of freedom (DOFs). External actions are applied on the solid boundary Γ , decomposed into a Dirichlet part Γ_D^u with imposed displacements $\bar{\mathbf{u}}$ and a Neumann part Γ_N^u with applied tractions $\bar{\mathbf{t}}(\mathbf{x}) \in \mathbb{R}^n$, where $\Gamma_D^u \cup \Gamma_N^u = \Gamma$ and $\Gamma_D^u \cap \Gamma_N^u = \emptyset$. Likewise, we may consider imposed micro-deformations $\bar{\boldsymbol{\chi}}$ on Γ_D^χ and applied double tractions $\bar{\mathbf{T}}(\mathbf{x}) \in \mathbb{R}^{n \times n}$ on Γ_N^χ , with $\Gamma_D^\chi \cup \Gamma_N^\chi = \Gamma$ and $\Gamma_D^\chi \cap \Gamma_N^\chi = \emptyset$. The body may also be subjected to volume forces $\mathbf{b}(\mathbf{x}) \in \mathbb{R}^n$ and double forces $\mathbf{M}(\mathbf{x}) \in \mathbb{R}^{n \times n}$.

2.2. Kinematics and balance laws

Assuming linearized kinematics, the first-order micromorphic continuum involves the following generalized strain measures:

$$\text{Compatible strain} \quad \boldsymbol{\varepsilon} = \text{sym } \nabla \mathbf{u}, \quad \varepsilon_{ij} = \frac{1}{2}(u_{i,j} + u_{j,i}); \quad (2)$$

$$\text{Relative strain} \quad \boldsymbol{\gamma} = \nabla \mathbf{u} - \boldsymbol{\chi}, \quad \gamma_{ij} = u_{i,j} - \chi_{ij}; \quad (3)$$

$$\text{Micro-deformation gradient} \quad \boldsymbol{\zeta} = \nabla \boldsymbol{\chi}, \quad \zeta_{ijk} = \chi_{ij,k}. \quad (4)$$

The power density of internal mechanical forces reads

$$p^{\text{int}} = \boldsymbol{\sigma} : \dot{\boldsymbol{\varepsilon}} + \boldsymbol{\tau} : \dot{\boldsymbol{\gamma}} + \boldsymbol{\mu} : \dot{\boldsymbol{\zeta}}, \quad (5)$$

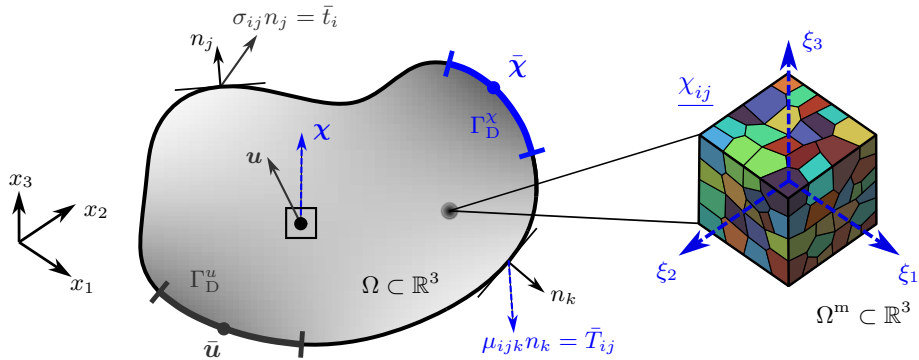


Figure 1: Schematic representation of a BVP in a micromorphic continuum (left) with a generic microstructure (right). The dashed blue arrows on the left represent second-order tensors. The first-order theory adopted in this work assumes that the micro-deformation χ_{ij} is homogeneous in Ω^m but varies in Ω .

where $\boldsymbol{\sigma}$ is the second-order, symmetric Cauchy stress tensor; $\boldsymbol{\tau}$ is the second-order, generally non-symmetric relative stress tensor; and $\boldsymbol{\mu}$ is the third-order double-stress tensor. Then, an appeal to the principle of virtual power [26] yields the following balance equations:

$$\text{Stress equilibrium} \quad \operatorname{div}(\boldsymbol{\sigma} + \boldsymbol{\tau}) + \mathbf{b} = \mathbf{0} \quad \text{in } \Omega, \quad (\boldsymbol{\sigma} + \boldsymbol{\tau}) \cdot \mathbf{n} = \bar{\mathbf{t}} \quad \text{on } \Gamma_N^u; \quad (6)$$

$$\text{Double stress equilibrium} \quad \operatorname{div} \boldsymbol{\mu} + \boldsymbol{\tau} + \mathbf{M} = \mathbf{0} \quad \text{in } \Omega, \quad \boldsymbol{\mu} \cdot \mathbf{n} = \bar{\mathbf{T}} \quad \text{on } \Gamma_N^\chi. \quad (7)$$

This system must be solved for the primary fields, $\mathbf{u} \in \mathbf{H}^1(\Omega; \mathbb{R}^n)$ and $\boldsymbol{\chi} \in \mathbf{H}^1(\Omega; \mathbb{R}^{n \times n})$, subject to boundary conditions $\mathbf{u} = \bar{\mathbf{u}}$ on Γ_D^u and $\boldsymbol{\chi} = \bar{\boldsymbol{\chi}}$ on Γ_D^χ .

2.3. Constitutive behavior

At this point, employing a traditional modeling approach requires closure relations between the generalized stresses and the conjugate generalized strains, i.e., a mapping $(\boldsymbol{\varepsilon}, \boldsymbol{\gamma}, \boldsymbol{\zeta}) \mapsto \{\boldsymbol{\sigma}, \boldsymbol{\tau}, \boldsymbol{\mu}\}(\boldsymbol{\varepsilon}, \boldsymbol{\gamma}, \boldsymbol{\zeta})$, a far from trivial requirement given the high-dimensional phase space. Indeed, even when assuming isotropic elasticity, micromorphic theories of degree one may require up to 18 parameters—of course, this general model is often simplified by means of kinematic assumptions, yielding reduced theories such as the micropolar model (with $\boldsymbol{\chi}$ purely skew-symmetric) [2], the microstrain model (with $\boldsymbol{\chi}$ purely symmetric) [3], or the relaxed micromorphic model (replacing $\nabla \boldsymbol{\chi}$ with the curvature part $\operatorname{curl} \boldsymbol{\chi}$) [27]. Still, as discussed thoroughly in the data-driven literature for both Cauchy [38, 62] and generalized [43, 45] continua, material behavior is, in principle, only known through an empirical dataset, be it experimental or from high-fidelity lower-scale simulations. Such data may not be accurately represented by a closed-form model with predefined functional form and material parameters, particularly for complex material behavior.

To address this problem in the context of generalized continua, we have recently presented a data-driven approach to micromorphic mechanics [45], where we assume that the material response is encoded in an empirical dataset in terms of generalized stress-strain coordinates $\{(\boldsymbol{\varepsilon}, \boldsymbol{\gamma}, \boldsymbol{\zeta}), (\boldsymbol{\sigma}, \boldsymbol{\tau}, \boldsymbol{\mu})\}$. Such data is employed directly to solve the fundamental equations (2)–(4) and (6)–(7) in BVPs without resorting to a constitutive model. However, the study considered synthetic data for proof-of-concept simulations, leaving the open question of whether the required generalized stress-strain data can be obtained from microstructured material responses in a practical scenario. The present work aims to fill this gap through a data-driven procedure for generalized material data identification, as described in section 4.

3. Data-driven computational mechanics for generalized continua

To set the stage for the data identification framework, let us briefly recall the data-driven problem for micromorphic mechanics [45]. Consider a discretization of the solid Ω into N nodes and M material points, achieved by a finite element procedure or another means. We assemble nodal displacement and external force vectors as $\underline{\mathbf{u}} = \{\mathbf{u}_a \in \mathbb{R}^n\}_{a=1}^N$ and $\underline{\mathbf{f}} = \{\mathbf{f}_a \in \mathbb{R}^n\}_{a=1}^N$, respectively. Similarly, the nodal micro-deformations and double forces are collected in vectors denoted as $\underline{\boldsymbol{\chi}} = \{\boldsymbol{\chi}_a \in \mathbb{R}^{n_\chi}\}_{a=1}^N$ and $\underline{\mathbf{m}} = \{\mathbf{m}_a \in \mathbb{R}^{n_\chi}\}_{a=1}^N$, respectively. Here, the size of the nodal micro-deformation vector, n_χ , depends on the symmetry conditions. For instance, $n_\chi = n^2$ for the full first-order micromorphic model and $n_\chi = n(n-1)/2$ for the micropolar case with $\boldsymbol{\chi}$ purely skew-symmetric.

In this section, second- and higher-order tensors evaluated at a point in space are expressed in their Voigt representation. Then, the discrete form of the kinematic relations (2)–(4) reads

$$\boldsymbol{\varepsilon}_e = \mathbf{B}_e^\varepsilon \underline{\mathbf{u}}, \quad (8)$$

$$\boldsymbol{\gamma}_e = \mathbf{B}_e^\gamma \underline{\mathbf{u}} - \mathbf{N}_e^\chi \underline{\boldsymbol{\chi}}, \quad (9)$$

$$\zeta_e = \mathbf{B}_e^\zeta \underline{\chi}, \quad (10)$$

while the balance equations (6)–(7) take the discrete forms

$$\sum_{e=1}^M w_e \left[\mathbf{B}_e^{\varepsilon^\top} \boldsymbol{\sigma}_e + \mathbf{B}_e^{\gamma^\top} \boldsymbol{\tau}_e \right] - \underline{\mathbf{f}} = \mathbf{0}, \quad (11)$$

$$\sum_{e=1}^M w_e \left[\mathbf{B}_e^{\zeta^\top} \boldsymbol{\mu}_e - \mathbf{N}_e^{\chi^\top} \boldsymbol{\tau}_e \right] - \underline{\mathbf{m}} = \mathbf{0}, \quad (12)$$

where $w_e \in \mathbb{R}$ is a standard integration weight; $\mathbf{N}_e^\chi \in \mathbb{R}^{n_\chi \times N n_\chi}$ is a shape function matrix for $\underline{\chi}$; and $\mathbf{B}_e^\varepsilon \in \mathbb{R}^{n_\varepsilon \times N n_\varepsilon}$, $\mathbf{B}_e^\gamma \in \mathbb{R}^{n_\gamma \times N n_\gamma}$, and $\mathbf{B}_e^\zeta \in \mathbb{R}^{n_\zeta \times N n_\zeta}$ are standard discretized gradient operators, with $n_\varepsilon = n(n+1)/2$ and $n_\zeta = n_\chi(n_\chi+1)/2$.

The state of the solid at a material point e is defined in terms of generalized coordinates \mathbf{z}_e in a local phase space Z_e , where we have, in general,

$$\mathbf{z}_e := (\boldsymbol{\varepsilon}_e, \boldsymbol{\gamma}_e, \boldsymbol{\zeta}_e, \boldsymbol{\sigma}_e, \boldsymbol{\tau}_e, \boldsymbol{\mu}_e) \in Z_e, \quad Z_e := \mathbb{R}^{n_\varepsilon} \times \mathbb{R}^{n_\gamma} \times \mathbb{R}^{n_\zeta} \times \mathbb{R}^{n_\varepsilon} \times \mathbb{R}^{n_\chi} \times \mathbb{R}^{n_\zeta}.$$

The local phase space is equipped with the metric

$$\|\mathbf{z}_e\|_e^2 := \frac{1}{2} \left(\mathbf{C}_e \boldsymbol{\varepsilon}_e \cdot \boldsymbol{\varepsilon}_e + \mathbf{C}_e^{-1} \boldsymbol{\sigma}_e \cdot \boldsymbol{\sigma}_e + \mathbf{D}_e \boldsymbol{\gamma}_e \cdot \boldsymbol{\gamma}_e + \mathbf{D}_e^{-1} \boldsymbol{\tau}_e \cdot \boldsymbol{\tau}_e + \mathbf{A}_e \boldsymbol{\zeta}_e \cdot \boldsymbol{\zeta}_e + \mathbf{A}_e^{-1} \boldsymbol{\mu}_e \cdot \boldsymbol{\mu}_e \right), \quad (13)$$

where $\mathbf{C}_e \in \mathbb{R}_{\text{sym},+}^{n_\varepsilon \times n_\varepsilon}$, $\mathbf{D}_e \in \mathbb{R}_{\text{sym},+}^{n_\gamma \times n_\gamma}$, and $\mathbf{A}_e \in \mathbb{R}_{\text{sym},+}^{n_\zeta \times n_\zeta}$ are positive-definite matrices representing numerical metric tensors (Appendix A). The local coordinates, collected as $\mathbf{z} := \{\mathbf{z}_e \in Z_e\}_{e=1}^M \in Z$, represent points in the global phase space $Z = Z_1 \times \dots \times Z_M$. The global distance metric then reads

$$\|\mathbf{z}\|^2 := \sum_{e=1}^M w_e \|\mathbf{z}_e\|_e^2. \quad (14)$$

With these definitions in hand, the data-driven micromorphic problem is given by

$$\min_{\bar{\mathbf{z}} \in D} \min_{\mathbf{z} \in E} \|\bar{\mathbf{z}} - \mathbf{z}\|^2 = \min_{\mathbf{z} \in E} \min_{\bar{\mathbf{z}} \in D} \|\bar{\mathbf{z}} - \mathbf{z}\|^2, \quad (15)$$

where $E \subset Z$ is the *generalized equilibrium set*

$$E := \{\mathbf{z} \in Z : (8)–(12)\}. \quad (16)$$

On the other hand, $D = D_1 \times \dots \times D_M$ is a global data set, where $D_e \subset Z_e$ denotes the local data set containing generalized stress–strain states accessible to the material point e .

4. Data identification for generalized continua

The framework discussed above relies on the availability of a suitable material data set D in terms of generalized coordinates $(\boldsymbol{\varepsilon}, \boldsymbol{\gamma}, \boldsymbol{\zeta}, \boldsymbol{\sigma}, \boldsymbol{\tau}, \boldsymbol{\mu})$. No consensus exists, to the best of our knowledge, on how such generalized stress–strain states may be obtained for microstructured materials exhibiting micromorphic phenomena. We thus aim to address this problem using a data-driven approach.

As in data-driven identification (DDI) for Cauchy continua [61, 62], we suppose that full-field displacement measurements are given for a BVP under various loading conditions. It is reasonable to assume the

availability of such measurements at a high resolution from micromechanical simulations or experimental images. In the present case of microstructured media, we further assume that the material has an identifiable representative volume Ω_m over which, considering a separation of scales, averaged microdeformations are also available. Examples of how such kinematic measures may arise are found in the literature [63, 64] and in our example in section 5.2. Then, we may construct a database consisting of discretized averaged displacements $\underline{\mathbf{u}}^\alpha = \{\mathbf{u}_a^\alpha \in \mathbb{R}^n\}_{a=1}^N$ and microdeformations $\underline{\mathbf{X}}^\alpha = \{\mathbf{X}_a^\alpha \in \mathbb{R}^{n_x}\}_{a=1}^N$ for each of the N_L loading conditions $\underline{\mathbf{f}}^\alpha = \{\mathbf{f}_a^\alpha \in \mathbb{R}^n\}_{a=1}^N$ and $\underline{\mathbf{m}}^\alpha = \{\mathbf{m}_a^\alpha \in \mathbb{R}^{n_x}\}_{a=1}^N$, indexed by $\alpha \in \{1, \dots, N_L\}$.

The objective of the proposed DDI framework is, then, to find a number \bar{N} of material states $\bar{\mathbf{z}}_i := (\bar{\varepsilon}_i, \bar{\gamma}_i, \bar{\zeta}_i, \bar{\sigma}_i, \bar{\tau}_i, \bar{\mu}_i)$ such that:

1. for each loading case α and material point e , it is possible to find generalized stresses $(\boldsymbol{\sigma}_e^\alpha, \boldsymbol{\tau}_e^\alpha, \boldsymbol{\mu}_e^\alpha)$ satisfying the balance equations (11) and (12);
2. for each loading case α , the generalized material state $\bar{\mathbf{z}}_{i_e^\alpha} = (\bar{\varepsilon}_{i_e^\alpha}, \bar{\gamma}_{i_e^\alpha}, \bar{\zeta}_{i_e^\alpha}, \bar{\sigma}_{i_e^\alpha}, \bar{\tau}_{i_e^\alpha}, \bar{\mu}_{i_e^\alpha})$ assigned to each material point e minimizes the distance to the mechanically admissible state $\mathbf{z}_e^\alpha = (\boldsymbol{\varepsilon}_e^\alpha, \boldsymbol{\gamma}_e^\alpha, \boldsymbol{\zeta}_e^\alpha, \boldsymbol{\sigma}_e^\alpha, \boldsymbol{\tau}_e^\alpha, \boldsymbol{\mu}_e^\alpha)$, according to the local metric (13).

Note that the mechanical strains $(\boldsymbol{\varepsilon}_e^\alpha, \boldsymbol{\gamma}_e^\alpha, \boldsymbol{\zeta}_e^\alpha)$ are known at every material point e from the available kinematic measurements $\underline{\mathbf{u}}^\alpha$ and $\underline{\mathbf{X}}^\alpha$ and the discrete kinematic relations (8)–(10).

We seek the two objectives above through the solution of the minimization problem

$$\min_{\{(\boldsymbol{\sigma}_e^\alpha, \boldsymbol{\tau}_e^\alpha, \boldsymbol{\mu}_e^\alpha)\}} \min_{\{\bar{\mathbf{z}}_i\}} \min_{\{i_e^\alpha\}} \left\{ \sum_{\alpha=1}^{N_L} \sum_{e=1}^M w_e \|\mathbf{z}_e^\alpha - \bar{\mathbf{z}}_{i_e^\alpha}\|_e^2 : \text{(8)}-\text{(12)} \quad \forall \alpha \in \{1, \dots, N_L\} \right\}, \quad (17)$$

where $i_e^\alpha \in \{1, \dots, \bar{N}\}$ represents an index pointer $(e, \alpha) \mapsto i_e^\alpha$ that assigns a data state $\bar{\mathbf{z}}_i$ to material point e in loading case α . Hereinafter, $\{\square_a^b\}$ denotes an array of all elements \square indexed by a and/or b .

Assuming that the mapping index $i_e^\alpha \in \{1, \dots, \bar{N}\}$ is given for all loading cases $\alpha \in \{1, \dots, N_L\}$ and material points $e \in \{1, \dots, M\}$, and imposing the balance equations (8)–(12) via Lagrange multipliers collected in vectors $\underline{\boldsymbol{\lambda}}^{u\alpha}$ and $\underline{\boldsymbol{\lambda}}^{x\alpha}$, the stationarity conditions with respect to $(\boldsymbol{\sigma}_e^\alpha, \boldsymbol{\tau}_e^\alpha, \boldsymbol{\mu}_e^\alpha, \underline{\boldsymbol{\lambda}}^{u\alpha}, \underline{\boldsymbol{\lambda}}^{x\alpha})$ read

$$w_e \mathbf{C}_e^{-1} (\boldsymbol{\sigma}_e^\alpha - \bar{\boldsymbol{\sigma}}_{i_e^\alpha}) - w_e \mathbf{B}_e^{\varepsilon\alpha} \underline{\boldsymbol{\lambda}}^{u\alpha} = \mathbf{0}, \quad (18)$$

$$w_e \mathbf{D}_e^{-1} (\boldsymbol{\tau}_e^\alpha - \bar{\boldsymbol{\tau}}_{i_e^\alpha}) - w_e \mathbf{B}_e^{\gamma\alpha} \underline{\boldsymbol{\lambda}}^{u\alpha} + w_e \mathbf{N}_e^{x\alpha} \underline{\boldsymbol{\lambda}}^{x\alpha} = \mathbf{0}, \quad (19)$$

$$w_e \mathbf{A}_e^{-1} (\boldsymbol{\mu}_e^\alpha - \bar{\boldsymbol{\mu}}_{i_e^\alpha}) - w_e \mathbf{B}_e^{\zeta\alpha} \underline{\boldsymbol{\lambda}}^{x\alpha} = \mathbf{0}, \quad (20)$$

$$\sum_{e=1}^M w_e \left[\mathbf{B}_e^{\varepsilon\alpha\top} \boldsymbol{\sigma}_e^\alpha + \mathbf{B}_e^{\gamma\alpha\top} \boldsymbol{\tau}_e^\alpha \right] - \underline{\mathbf{f}}^\alpha = \mathbf{0}, \quad (21)$$

$$\sum_{e=1}^M w_e \left[\mathbf{B}_e^{\zeta\alpha\top} \boldsymbol{\mu}_e^\alpha - \mathbf{N}_e^{x\alpha\top} \boldsymbol{\tau}_e^\alpha \right] - \underline{\mathbf{m}}^\alpha = \mathbf{0}. \quad (22)$$

Combining equations (18)–(20) and (21)–(22) gives a linear system in $(\underline{\boldsymbol{\lambda}}^{u\alpha}, \underline{\boldsymbol{\lambda}}^{x\alpha}) \forall \alpha \in \{1, \dots, N_L\}$:

$$\begin{aligned} & \sum_{e=1}^M w_e \left[\mathbf{B}_e^{\varepsilon\alpha\top} \mathbf{C}_e \mathbf{B}_e^{\varepsilon\alpha} + \mathbf{B}_e^{\gamma\alpha\top} \mathbf{D}_e \mathbf{B}_e^{\gamma\alpha} \right] \underline{\boldsymbol{\lambda}}^{u\alpha} - \sum_{e=1}^M w_e \left[\mathbf{B}_e^{\gamma\alpha\top} \mathbf{D}_e \mathbf{N}_e^{x\alpha} \right] \underline{\boldsymbol{\lambda}}^{x\alpha} \\ &= \underline{\mathbf{f}}^\alpha - \sum_{e=1}^M w_e \left[\mathbf{B}_e^{\varepsilon\alpha\top} \bar{\boldsymbol{\sigma}}_{i_e^\alpha} + \mathbf{B}_e^{\gamma\alpha\top} \bar{\boldsymbol{\tau}}_{i_e^\alpha} \right], \end{aligned} \quad (23)$$

$$\begin{aligned}
& \sum_{e=1}^M w_e \left[\mathbf{N}_e^{\chi\alpha} \mathbf{\Gamma} \mathbf{D}_e \mathbf{B}_e^{\gamma\alpha} \right] \boldsymbol{\lambda}^{u\alpha} - \sum_{e=1}^M w_e \left[\mathbf{B}_e^{\zeta\alpha} \mathbf{\Gamma} \mathbf{A}_e \mathbf{B}_e^{\zeta\alpha} + \mathbf{N}_e^{\chi\alpha} \mathbf{\Gamma} \mathbf{D}_e \mathbf{N}_e^{\chi\alpha} \right] \boldsymbol{\lambda}^{\chi\alpha} \\
&= \sum_{e=1}^M w_e \left[\mathbf{B}_e^{\zeta\alpha} \mathbf{\Gamma} \bar{\boldsymbol{\mu}}_{i_e^\alpha} - \mathbf{N}_e^{\chi\alpha} \mathbf{\Gamma} \bar{\boldsymbol{\tau}}_{i_e^\alpha} \right] - \underline{\mathbf{m}}^\alpha.
\end{aligned} \tag{24}$$

The coupled equations (23)–(24) are standard forms analogous to linear micromorphic elasticity with particular right-hand sides, and can thus be easily implemented in conventional finite element programs. The mechanical stresses are then updated locally from (18)–(20).

On the other hand, stationarity with respect to the material state $\bar{\mathbf{z}}_i$ gives, $\forall i \in \{1, \dots, \bar{N}\}$,

$$\sum_{\alpha=1}^{N_L} \sum_{e \in S_i^\alpha} w_e \mathbf{C}_e (\boldsymbol{\varepsilon}_e^\alpha - \bar{\boldsymbol{\varepsilon}}_{i_e^\alpha}) = \mathbf{0}, \quad \sum_{\alpha=1}^{N_L} \sum_{e \in S_i^\alpha} w_e \mathbf{C}_e^{-1} (\boldsymbol{\sigma}_e^\alpha - \bar{\boldsymbol{\sigma}}_{i_e^\alpha}) = \mathbf{0}, \tag{25}$$

$$\sum_{\alpha=1}^{N_L} \sum_{e \in S_i^\alpha} w_e \mathbf{D}_e (\boldsymbol{\gamma}_e^\alpha - \bar{\boldsymbol{\gamma}}_{i_e^\alpha}) = \mathbf{0}, \quad \sum_{\alpha=1}^{N_L} \sum_{e \in S_i^\alpha} w_e \mathbf{D}_e^{-1} (\boldsymbol{\tau}_e^\alpha - \bar{\boldsymbol{\tau}}_{i_e^\alpha}) = \mathbf{0}, \tag{26}$$

$$\sum_{\alpha=1}^{N_L} \sum_{e \in S_i^\alpha} w_e \mathbf{A}_e (\boldsymbol{\zeta}_e^\alpha - \bar{\boldsymbol{\zeta}}_{i_e^\alpha}) = \mathbf{0}, \quad \sum_{\alpha=1}^{N_L} \sum_{e \in S_i^\alpha} w_e \mathbf{A}_e^{-1} (\boldsymbol{\mu}_e^\alpha - \bar{\boldsymbol{\mu}}_{i_e^\alpha}) = \mathbf{0}, \tag{27}$$

where

$$S_i^\alpha = \{e \in \{1, \dots, M\} : i_e^\alpha = i\} \tag{28}$$

is a set of material point indices associated with the data state i and snapshot α . We thus find from (25)–(27) that the i th identified material data state $\bar{\mathbf{z}}_i$ is a weighted average of a subset of the mechanically admissible states $\{\mathbf{z}_e^\alpha\}$, restricted to material points and snapshots to which the data state i has been assigned. Moreover, combining equations (18)–(20) and (25)–(27) gives, $\forall i \in \{1, \dots, \bar{N}\}$,

$$\sum_{\alpha=1}^{N_L} \sum_{e \in S_i^\alpha} w_e \mathbf{B}_e^{\varepsilon\alpha} \boldsymbol{\lambda}^{u\alpha} = \mathbf{0}, \tag{29}$$

$$\sum_{\alpha=1}^{N_L} \sum_{e \in S_i^\alpha} w_e (\mathbf{B}_e^{\gamma\alpha} \boldsymbol{\lambda}^{u\alpha} - \mathbf{N}_e^{\chi\alpha} \boldsymbol{\lambda}^{\chi\alpha}) = \mathbf{0}, \tag{30}$$

$$\sum_{\alpha=1}^{N_L} \sum_{e \in S_i^\alpha} w_e \mathbf{B}_e^{\zeta\alpha} \boldsymbol{\lambda}^{\chi\alpha} = \mathbf{0}. \tag{31}$$

Accordingly, the Lagrange multipliers are such that the corresponding generalized pseudo-strains have a zero w_e -weighted average. Finally, stationarity with respect to $\{i_e^\alpha\}$ corresponds to finding the set of indices assigned to each material point e and load case α such that the distance between the material and mechanical states is minimized. Here, as suggested in Stainier et al. [62] for Cauchy continua, minimization with respect to $(\{\bar{\mathbf{z}}_i\}, \{i_e^\alpha\})$ is performed simultaneously through k -means clustering. We present the computational procedure in Algorithm 1. Note that algorithmic convergence of DDI towards a unique solution has been assessed for the Cauchy case in Hachem et al. [65] (see also Leygue [66]).

5. Numerical simulations

This section presents numerical simulations demonstrating the capability of the proposed framework to identify *generalized* material states from heterogeneous kinematic field data and applied forces. Specifically, our approach enables the faithful identification of non-trivial features in generalized stresses, such as

Algorithm 1 Alternate minimization scheme for problem (17).

- 1: Initialize iterations with $j := 0$.
- 2: Perform k -means clustering on $\{(\boldsymbol{\varepsilon}_e^\alpha, \boldsymbol{\gamma}_e^\alpha, \boldsymbol{\zeta}_e^\alpha)\}$ to find initial data estimates $\{(\bar{\boldsymbol{\varepsilon}}_i, \bar{\boldsymbol{\gamma}}_i, \bar{\boldsymbol{\zeta}}_i)\}^{(0)}$ and $\{i_e^\alpha\}^{(0)}$.
- 3: Set an initial guess $\{(\bar{\boldsymbol{\sigma}}_i, \bar{\boldsymbol{\tau}}_i, \bar{\boldsymbol{\mu}}_i)\}^{(0)}$.
- 4: **repeat**
- 5: Set $j \leftarrow j + 1$.
- 6: With fixed $\{\bar{\mathbf{z}}_i\}^{(j-1)}$ and $\{i_e^\alpha\}^{(j-1)}$, find $(\boldsymbol{\lambda}^{u\alpha}, \boldsymbol{\lambda}^{\chi\alpha})^{(j)}$ from (23)–(24) $\forall \alpha \in \{1, \dots, N_L\}$ and update $(\boldsymbol{\sigma}_e^\alpha, \boldsymbol{\tau}_e^\alpha, \boldsymbol{\mu}_e^\alpha)^{(j)}$ from (18)–(20) $\forall \alpha \in \{1, \dots, N_L\}$ and $e \in \{1, \dots, M\}$.
- 7: Perform k -means clustering on $\{\mathbf{z}_e^\alpha\}^{(j)}$ to update the material data $\{\bar{\mathbf{z}}_i\}^{(j)}$ and $\{i_e^\alpha\}^{(j)}$.
- 8: **until** $\{i_e^\alpha\}^{(j)} = \{i_e^\alpha\}^{(j-1)}$.
- 9: Set $\{(\boldsymbol{\sigma}_e^\alpha, \boldsymbol{\tau}_e^\alpha, \boldsymbol{\mu}_e^\alpha)\} := \{(\boldsymbol{\sigma}_e^\alpha, \boldsymbol{\tau}_e^\alpha, \boldsymbol{\mu}_e^\alpha)\}^{(j)}$ and $\{\bar{\mathbf{z}}_i\} := \{\bar{\mathbf{z}}_i\}^{(j)}$ (identified material data).

non-symmetric and higher-order components. We assess the representativeness of the identified material data for accurately characterizing the mechanical response in BVPs of non-standard continua.

5.1. Validation with synthetic micromorphic data

First, as a proof of concept, a synthetic study is performed using data from a numerical BVP in which the material behavior follows a full micromorphic constitutive model, i.e., one that includes both symmetric and skew-symmetric microdeformations. Specifically, a specimen with geometrical defects is employed, consisting of a plate with three holes under plane strain conditions (Figure 2). The sample is meshed using $N = 1778$ nodes and 1688 bilinear quadrilateral elements (i.e., $M = 6752$ material points). We assume the material obeys a micromorphic elasticity constitutive model, characterized by a strain energy density

$$\psi(\boldsymbol{\varepsilon}, \boldsymbol{\gamma}, \boldsymbol{\zeta}) = \frac{1}{2} (\mathbf{C} \boldsymbol{\varepsilon} : \boldsymbol{\varepsilon} + \mathbf{D} \boldsymbol{\gamma} : \boldsymbol{\gamma} + \mathbf{A} \boldsymbol{\zeta} : \boldsymbol{\zeta}). \quad (32)$$

As such, the constitutive relations

$$\boldsymbol{\sigma} = \frac{\partial \psi}{\partial \boldsymbol{\varepsilon}} = \mathbf{C} \boldsymbol{\varepsilon}, \quad \boldsymbol{\tau} = \frac{\partial \psi}{\partial \boldsymbol{\gamma}} = \mathbf{D} \boldsymbol{\gamma}, \quad \boldsymbol{\mu} = \frac{\partial \psi}{\partial \boldsymbol{\zeta}} = \mathbf{A} \boldsymbol{\zeta} \quad (33)$$

naturally follow and provide closure to the governing equations (2)–(7). The constitutive tensors are assumed to have the form (A.3), with Young's modulus $E = 217.5$ GPa and Poisson's ratio $\nu = 0.3$ (i.e.,

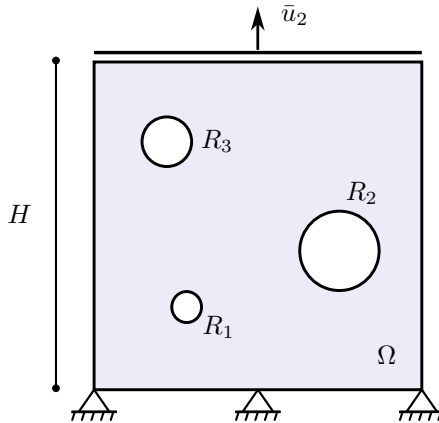


Figure 2: Boundary value problem for the perforated plate with a micromorphic material under plane strain conditions. The holes with radii $R_1 = 0.045H$, $R_2 = 0.12H$, and $R_3 = 0.075H$ are located at coordinates $(0.28, 0.25)H$, $(0.72, 0.42)H$, and $(0.22, 0.75)H$, respectively, measured from the bottom-left corner. We assume $H = 10$ mm in the simulations.

$\lambda = 125.48$ GPa, $\mu = 83.65$ GPa). We further set $c_1 = 4.26$, $\kappa_1 = 713.26$ GPa, and $\ell = 2/\sqrt{2}$ mm.

Finite element simulations are conducted imposing displacements \bar{u}_2 in $N_L = 30$ increments from 0 to 1 mm. The microdeformations are set free on the boundary. At each load step, snapshots of the kinematic fields are recorded in the form of nodal displacements and microdeformations $(\mathbf{u}, \mathbf{\chi})$, together with the corresponding reaction forces on the top side. Figure 3 shows a snapshot of the kinematics at $\bar{u}_2 = 1$ mm. Note, in particular, the non-symmetric microdeformation components χ_{ij} arising from the polar coupling modulus κ_1 . The mechanical generalized strains $(\boldsymbol{\varepsilon}_e, \boldsymbol{\gamma}_e, \boldsymbol{\zeta}_e)$ then follow locally from (8)–(10).

This simulated data is passed to the DDI solver to obtain the corresponding stress fields and build a representative material dataset. We select the metric tensors of the form (A.3) and choose, as numerical (hyper)parameters different from the constitutive model, $E = 100$ GPa and $\nu = 0.35$ (i.e., $\lambda = 86.42$ GPa, $\mu = 37.04$ GPa), $c_1 = 5$, and $\kappa_1 = 37.04$ GPa. We note that an objective choice of metric parameters, free from parameter bias, consists of finding optimal values (Appendix A); this approach is not implemented here for the sake of simplicity. Finally, we set the number of data points to be identified as $\bar{N} = 2026$, i.e., a ratio of mechanical states to material states $(MN_L)/\bar{N} \approx 100$.

Figure 4 shows the generalized second-order stress fields $\sigma_{ij} + \tau_{ij}$ at $\bar{u}_2 = 1$ mm, comparing the identified mechanical states to the reference constitutive model. While a very slight noise level is observed, the contour plots show remarkable agreement between the identified and reference fields. In particular, the non-symmetric nature of τ_{ij} is properly identified. Moreover, although an overestimation of $\sigma_{11} + \tau_{11}$ is present along the bottom edge, the stress concentrations show good agreement in both location and magnitude. Figure 5 presents the generalized third-order stress fields μ_{ijk} , again contrasting the identified mechanical states with the reference constitutive response. The level of noise in the identified response is more significant than for the second-order components. Nevertheless, excellent agreement is still observed,

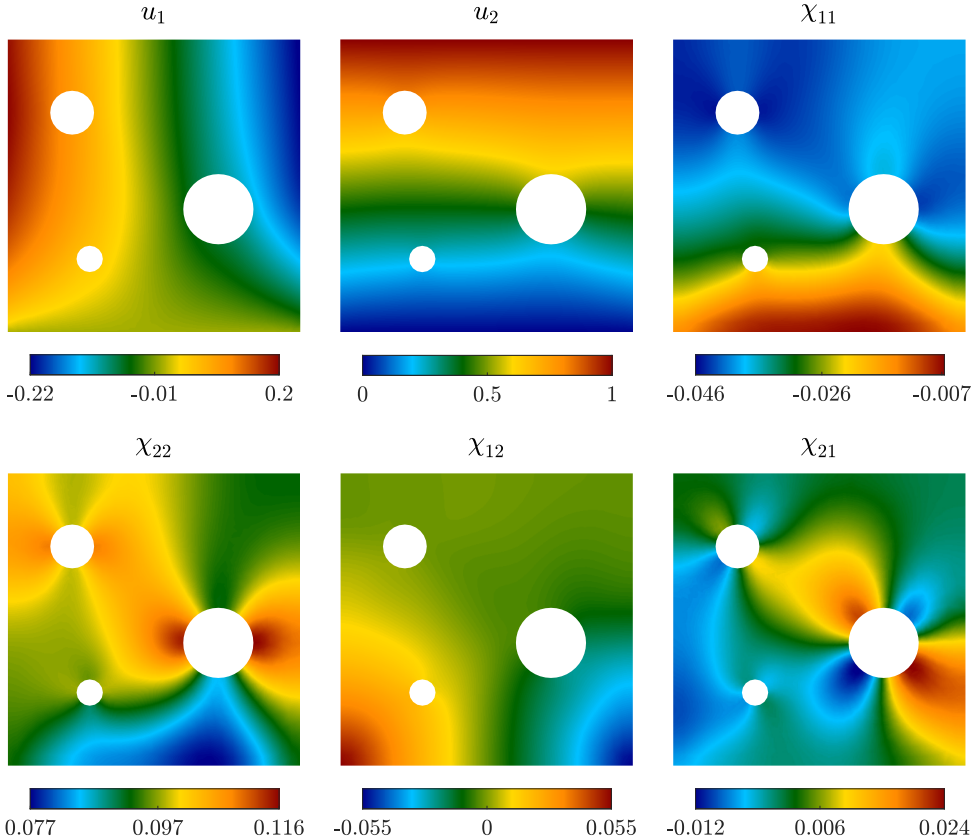


Figure 3: Kinematic data: displacements u_i [mm] and non-symmetric microdeformations χ_{ij} at $\bar{u}_2 = 1$ mm.

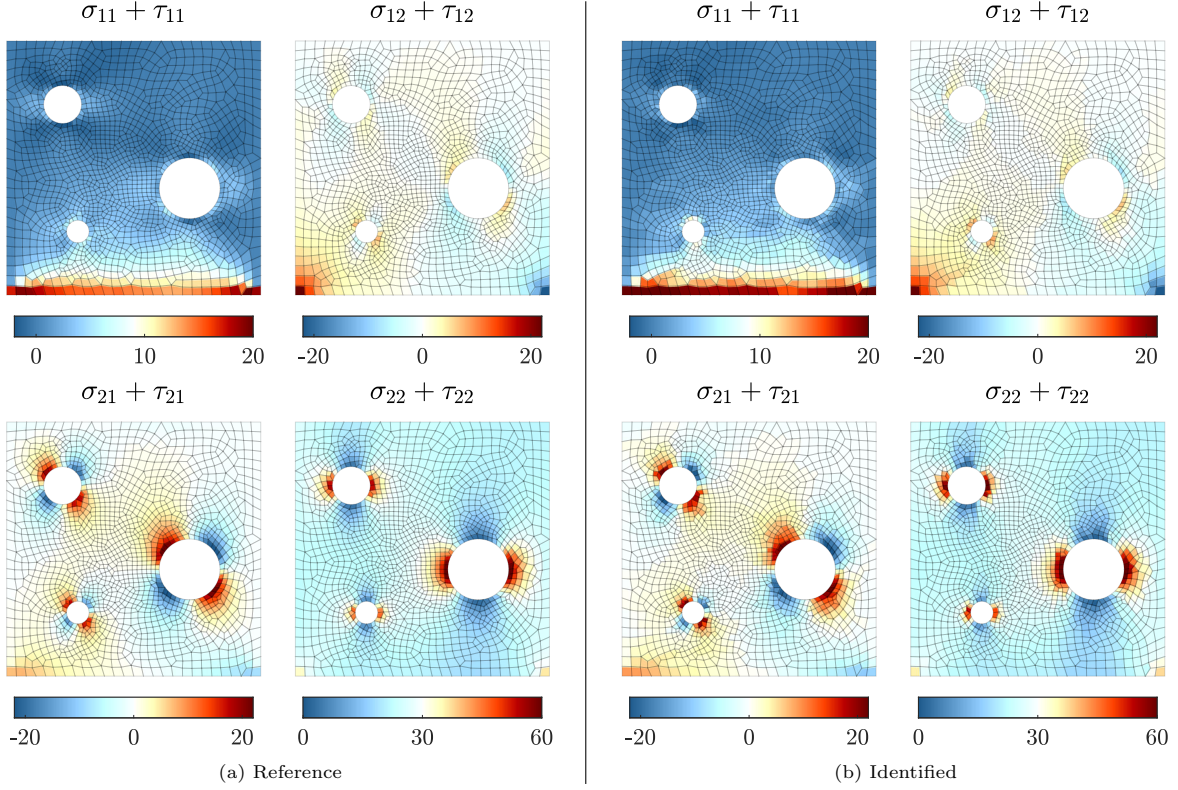


Figure 4: Comparison of second-order generalized stress fields $\sigma_{ij} + \tau_{ij}$ [GPa], showing (a) the ground-truth reference simulation and (b) the identified mechanical stress fields.

both in terms of spatial distribution and magnitude of the different third-order components.

Recall that in the reference constitutive model, the volumetric and deviatoric parts of the classical stress-strain relation $\boldsymbol{\sigma} = \mathbf{C}\boldsymbol{\epsilon}$; the volumetric, symmetric-deviatoric, and skew-symmetric parts of the relative stress-strain relation $\boldsymbol{\tau} = \mathbf{D}\boldsymbol{\gamma}$; and the volumetric, symmetric-deviatoric, and skew-symmetric gradient parts of the higher-order relation $\boldsymbol{\mu} = \mathbf{A}\boldsymbol{\zeta}$ (with the decomposition taken over the first two indices) are all linear. Figure 6 shows representative point clouds on the associated phase-space planes, considering all generalized stress-strain components. Specifically, we plot the identified data points and compare them to the expected linear behavior from the ground-truth simulations. We observe that the identified material states $\{\bar{\mathbf{z}}_i\}$, corresponding to cluster centroids of the identified mechanical states $\{\mathbf{z}_e^\alpha\}$,

Table 1: Reference linear relations and summary statistics of the identified data: R^2 values from least-squares regression and relative errors with respect to reference constitutive parameters.

Relation	Fig. 6	Ref. slope	R^2	Slope error [%]
$(\sigma_{11} + \sigma_{22})/(\varepsilon_{11} + \varepsilon_{22})$	(a1)	$2(\lambda + \mu)$	0.98	3.53
$\sigma_{12}/\varepsilon_{12}$	(a2)	2μ	0.97	19.06
$(\tau_{11} + \tau_{22})/(\gamma_{11} + \gamma_{22})$	(b1)	$2c_1(\lambda + \mu)$	0.91	6.34
$(\tau_{12} + \tau_{21})/(\gamma_{12} + \gamma_{21})$	(b2)	$2c_1\mu$	0.93	3.48
$(\tau_{21} - \tau_{12})/(\gamma_{21} - \gamma_{12})$	(b3)	κ_1	0.93	13.67
$(\mu_{111} + \mu_{112} + \mu_{221} + \mu_{222})/(\zeta_{111} + \zeta_{112} + \zeta_{221} + \zeta_{222})$	(c1)	$2\ell^2(\lambda + \mu)$	0.85	0.98
$(\mu_{121} + \mu_{122} + \mu_{211} + \mu_{212})/(\zeta_{121} + \zeta_{122} + \zeta_{211} + \zeta_{212})$	(c2)	$2\mu\ell^2$	0.85	8.42
$(\mu_{211} + \mu_{212} - \mu_{121} - \mu_{122})/(\zeta_{211} + \zeta_{212} - \zeta_{121} - \zeta_{122})$	(c3)	$2\mu\ell^2$	0.86	10.72

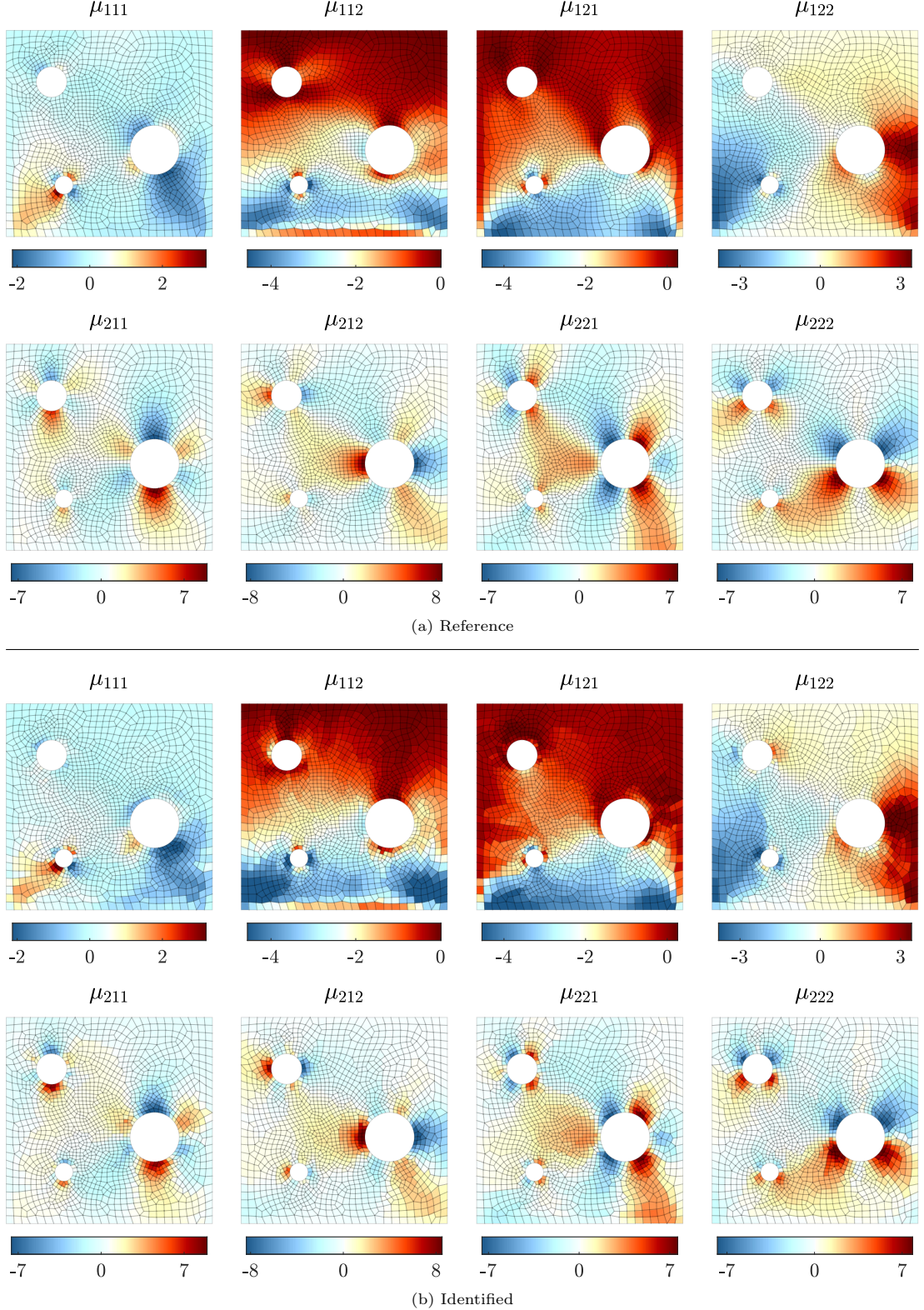


Figure 5: Comparison of third-order generalized stress fields μ_{ijk} [GPa · mm], showing (a) the ground-truth reference simulation and (b) the identified mechanical stress fields.

align closely with the ground-truth model. Nevertheless, some spread around the reference behavior is obtained due to the heterogeneity of the input fields (cf. [62]).

Table 1 reports the correlation values for each linear pair, as well as the relative error in the corresponding expected slopes. The high R^2 values indicate that the linear behavior is well captured. The predicted

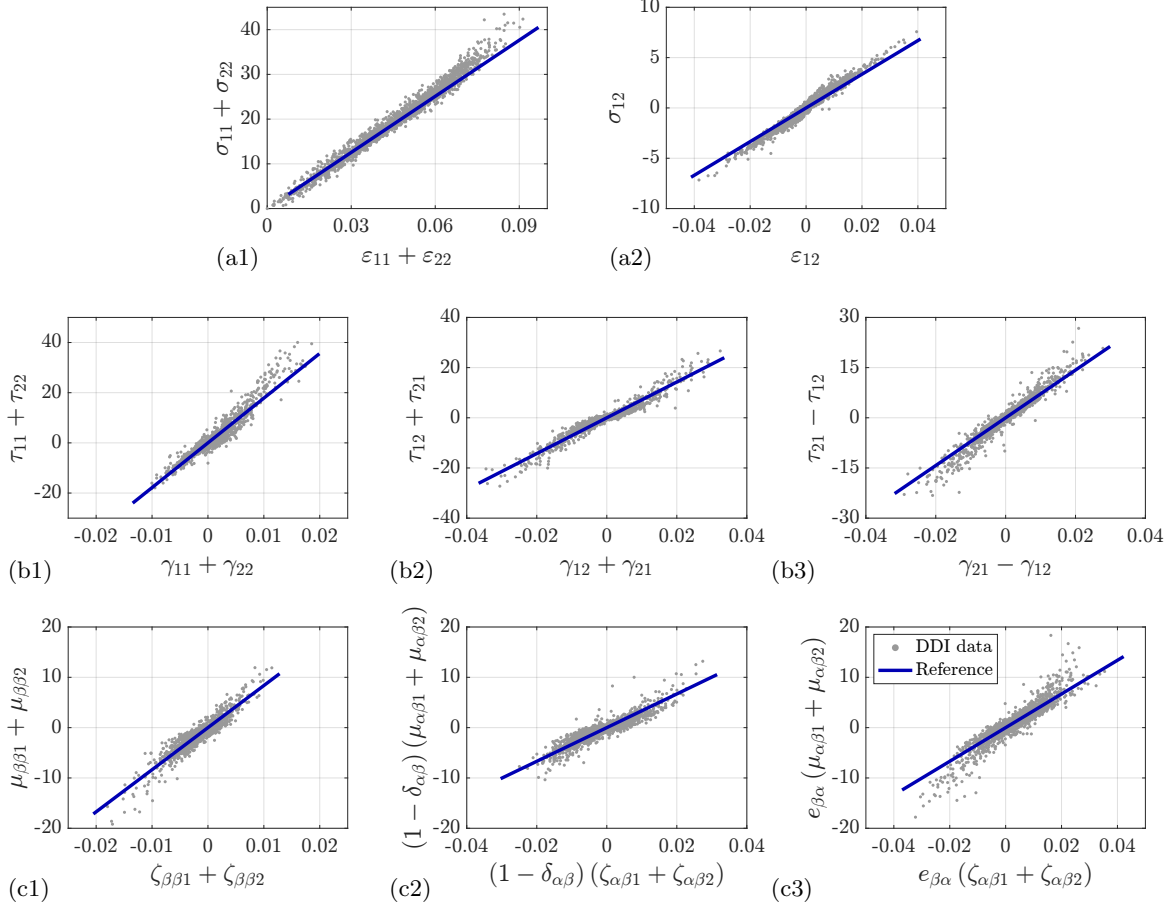


Figure 6: Material states identified from all snapshots of the perforated plate (gray, DDI data) and expected linear behavior from the ground-truth constitutive model (blue). Note that summation over repeated indices is assumed, where $\alpha, \beta \in \{1, 2\}$. Stress quantities are shown in GPa. See Table 1 for representative statistics.

slopes, obtained via least-squares fitting of the data points, closely approximate the expected values from the linear relations, with the highest relative error observed for the $(\varepsilon_{12}, \sigma_{12})$ components. Specifically, as visible in Figure 6b3, the corresponding data points align more steeply at small shear stress/strain values, leading to an overestimation of the slope in a least-squares fit. A similar effect, albeit to a lesser degree, is observed for the skew-symmetric components in figures 6b3 and 6c3, while all the other components show a much closer slope agreement. These observations notwithstanding, we emphasize that the objective of the proposed framework is to remain model-free; accordingly, we aim to identify relevant data points rather than material parameters. Indeed, the methodology remains applicable in practical scenarios where the ground-truth constitutive model is unknown and may be non-linear.

5.2. Identification and prediction for mechanical metamaterials

As an example of application, the proposed framework is now used to identify and predict the behavior of mechanical metamaterials in a reduced phase space. Specifically, we consider BVPs where the material is composed of an elastic honeycomb lattice (Figure 7). Suppose the base lattice material obeys Euler–Bernoulli beam theory. Then, zeroth-order variational homogenization [67] yields an explicit effective strain energy density that serves as the reference model for the continuum behavior of the metastructure:

$$\psi(\boldsymbol{\varepsilon}, \boldsymbol{\gamma}) = \frac{1}{2} (\mathbf{C} \boldsymbol{\varepsilon} : \boldsymbol{\varepsilon} + \kappa_1 \text{skw} \boldsymbol{\gamma} : \text{skw} \boldsymbol{\gamma}) = \frac{1}{2} \mathbf{C} \boldsymbol{\varepsilon} : \boldsymbol{\varepsilon} + \kappa_1 ((\text{curl } \mathbf{u})_3/2 - \theta_3)^2, \quad (34)$$

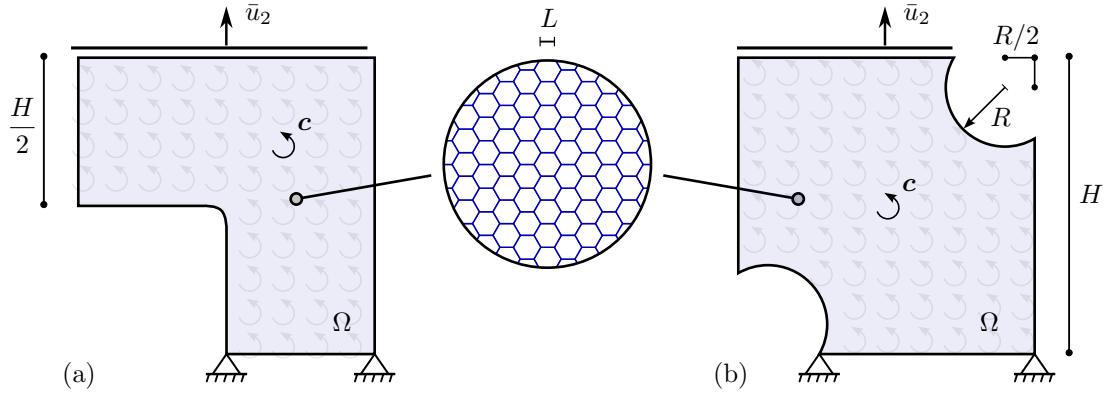


Figure 7: Schematic representation of boundary value problems with a honeycomb microstructure: (a) L-shaped specimen used for material identification, and (b) double-notched specimen used for data-driven predictions. We assume $H = 30$ mm and $R = 6$ mm. The L-shaped specimen includes a small fillet of radius 0.75 mm at the inner corner.

where, in 2D, $(\text{skw } \boldsymbol{\gamma})_{21} = (\text{curl } \mathbf{u})_3/2 - \theta_3$, with $(\text{curl } \mathbf{u})_3 = u_{2,1} - u_{1,2}$, while $\theta_3 = (\chi_{21} - \chi_{12})/2$ is an out-of-plane microrotation field. The effective moduli are given in Voigt form by

$$C_{11} = \frac{EA (EAL^2 + 36EI)}{2\sqrt{3} (EAL^3 + 12EIL)}, \quad C_{12} = \frac{EA (EAL^2 - 12EI)}{2\sqrt{3} (EAL^3 + 12EIL)}, \quad C_{33} = \frac{4\sqrt{3} EA EI}{EAL^3 + 12EIL}, \quad (35)$$

while the polar modulus reads

$$\kappa_1 = \frac{4\sqrt{3} EI}{L^3}, \quad (36)$$

where E , A , I , and L denote the Young's modulus, cross-sectional area, moment of inertia, and length of the beams comprising the microstructure. This homogenized model Γ -converges to the behavior of the discrete metastructure in the continuum limit $\epsilon \rightarrow 0$, where ϵ denotes the ratio between the unit cell size and the characteristic size of the macroscopic domain [67, 68].

A key feature of this model is the form of the microdeformation tensor,

$$\chi_{ij} = -e_{ijk} \theta_k \quad (3D), \quad \chi_{\alpha\beta} = -e_{\alpha\beta} \theta_3 \quad (2D), \quad (37)$$

where e_{ijk} and $e_{\alpha\beta}$ denote the components of the Levi-Civita permutation tensor in 3D and 2D, respectively. Thus, the continuum microdeformations arise physically from joint rotations within the lattice and are purely skew-symmetric. Moreover, the model (34) corresponds to a particular generalized continuum of order zero—a micropolar model independent of curvature effects, and thus insensitive to the length-scale ϵ (see Ulloa et al. [17] for higher-order generalizations of the theory and size effects).

This explicit analytical setting supplied by the homogenization theory is convenient for benchmarking the proposed identification framework against reference solutions. Here, the phase-space coordinates are reduced to the quadruple $(\boldsymbol{\epsilon}, \boldsymbol{\gamma}, \boldsymbol{\sigma}, \boldsymbol{\tau})$. We proceed with data identification from a BVP in this reduced phase space, followed by predictions in an unseen BVP using the identified dataset.

5.2.1. Data identification

Consider the L-shaped specimen shown in Figure 7a. At the lattice scale, the honeycomb metamaterial is comprised of straight beams with Young's modulus $E = 430$ MPa, cross-sectional area $A = 0.2$ mm 2 , second moment of inertia $I = 6.67 \times 10^{-4}$ mm 4 , and length $L = 2$ mm, leading to homogenized model parameters $\lambda = 12.167$ MPa, $\mu = 0.246$ MPa, and $\kappa_1 = 0.248$ MPa (equations (34)–(36)). The bottom side is fixed in both directions, while vertical displacements \bar{u}_2 are applied to the top side in $N_L = 30$

increments from 0 to 1 mm. Moreover, a uniformly distributed body couple $\mathbf{c} = c \mathbf{e}_3$ is applied in the out-of-plane direction, such that, in equation (7),

$$M_{ij} = -e_{ijk} c_k. \quad (38)$$

This body couple could arise, for example, from the action of a horizontal magnetic field $\mathbf{B} = B \mathbf{e}_1$ on vertically aligned dipoles $\mathbf{m} = m \mathbf{e}_2$ distributed over the joints of the lattice. In the honeycomb geometry, each unit cell contains two node types [67]. Denoting the unit cell volume by V , the resulting body couple per unit volume is

$$\mathbf{c} = \frac{2}{V} \mathbf{m} \times \mathbf{B} = -\frac{2}{V} m B \mathbf{e}_3, \quad V = \frac{3\sqrt{3}}{2} L^2. \quad (39)$$

Here, we set $mB = 0.03$ N mm, corresponding to a distributed couple magnitude $c = -0.0058$ N/mm².

Recall that the discrete model, with domain size and applied displacement scaled by ϵ , must converge to the homogenized model response as $\epsilon \rightarrow 0$. Figure 8 shows a snapshot of the kinematics at $\bar{u}_2 = 1$ mm, demonstrating very close agreement between the discrete (direct) numerical simulation at $\epsilon = 1/90$ and the homogenized model. The continuum mesh contains 3749 nodes and 3626 bilinear quads. At each load step, snapshots of the kinematic fields are recorded in the form of nodal displacements and microdeformations ($\mathbf{u}, \underline{\chi}$), together with the corresponding reaction forces and reaction couples on the top side. Here, the nodal microdeformations $\underline{\chi}$ are given in terms of discrete out-of-plane microrotations θ_3 , according to equation (37). The generalized strains ($\boldsymbol{\varepsilon}_e, \boldsymbol{\gamma}_e$) then follow locally from equations (8)–(9).

We pass the recorded data to the identification solver to obtain the corresponding stress fields and representative material dataset, which will be benchmarked against the homogenized model solution. The metric tensors are chosen according to (A.3), with numerical (hyper)parameters, different from those of the homogenized model, set as $\lambda = 50$ MPa, $\mu = 1$ MPa, and $\kappa_1 = 1$ MPa. Again, recall that the optimal

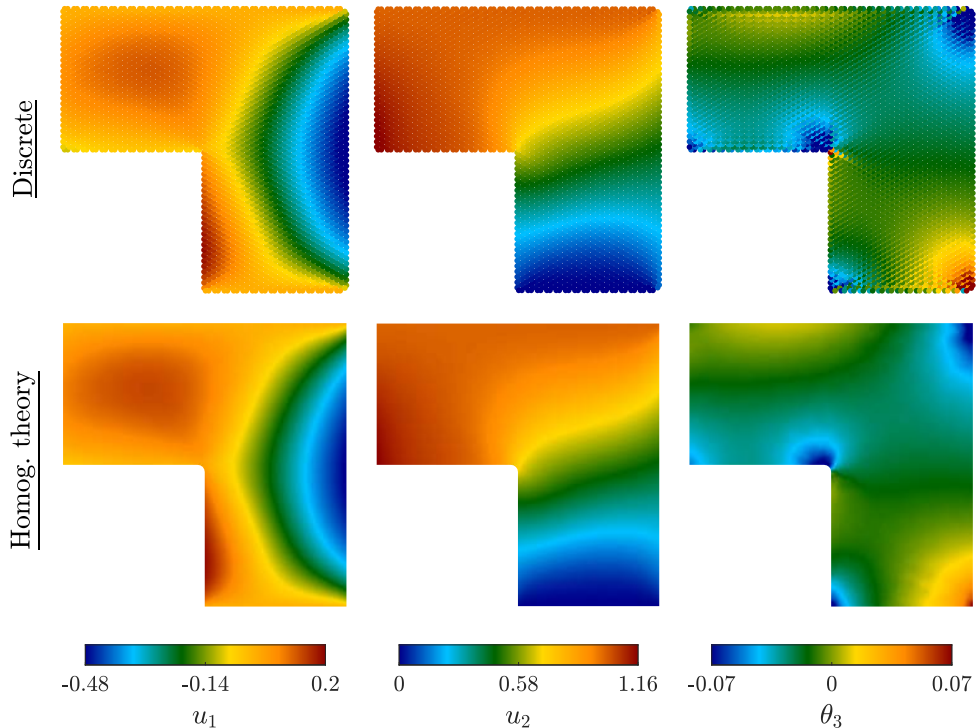


Figure 8: Kinematic data: components u_i [mm] and microrotations θ_3 of the honeycomb L-shaped specimen at $\bar{u}_2 = 1$ mm, showing the direct numerical simulation of the discrete metastructure (top) and the homogenized model (bottom).

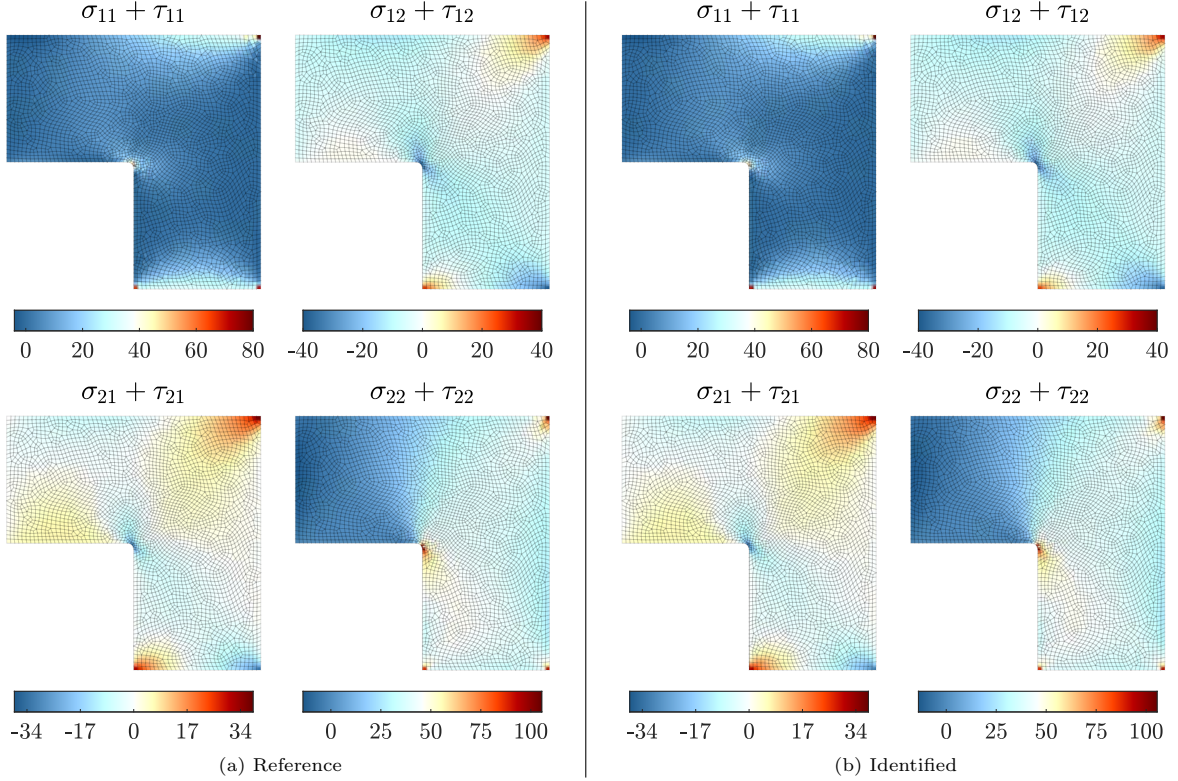


Figure 9: Comparison of generalized stress fields $\sigma_{ij} + \tau_{ij}$ [kPa] in the honeycomb L-shaped specimen, showing (a) the ground-truth homogenized model simulation and (b) the identified mechanical stress fields.

metric parameters may also be chosen objectively (Appendix A). Finally, we set the number of data points to be identified as $\bar{N} = 4352$, with a ratio of mechanical states to material states $(MN_L)/\bar{N} \approx 100$.

Figure 9 shows the generalized stress fields $\sigma_{ij} + \tau_{ij}$ at $\bar{u}_2 = 1$ mm, comparing the identified mechanical states to the reference homogenized model. We observe an excellent agreement throughout the domain for all components, accurately capturing the non-symmetry of $\sigma_{ij} + \tau_{ij}$ induced by the applied body couple. The identified material data points are shown together with the expected linear relations in Figure 10. The identified material states $\{\bar{\mathbf{z}}_i\}$ (gray dots), corresponding to cluster centroids of the identified mechanical states $\{\mathbf{z}_e^\alpha\}$, align closely with the ground-truth homogenized model. The spread around the reference, most pronounced for the $\sigma_{11} + \sigma_{22}$ component, reflects the heterogeneity of the input fields. Table 2 reports the correlation values for the linear pairs and the relative errors in the corresponding relations. As expected from the stress contour plots, high R^2 values are observed for $\sigma_{11} + \sigma_{22}$ and σ_{12} , properly capturing the linear response. Moreover, the relative stress $\tau_{21} - \tau_{12}$ is expected to be virtually constant, as defined by

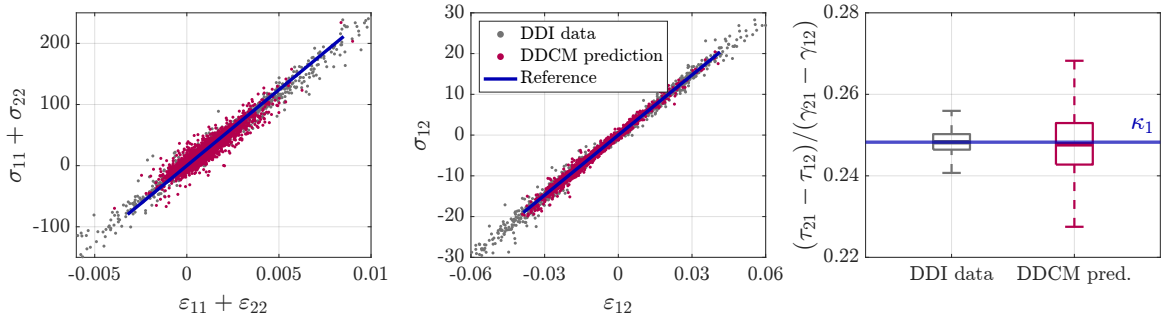


Figure 10: Material states identified from all snapshots of the honeycomb L-shaped specimen (gray, DDI data), data-driven predictions in the honeycomb double-notched specimen (red, DDCM prediction), and expected linear behavior from the homogenized model (blue). Stress quantities are shown in kPa. See tables 2 and 3 for representative statistics.

Table 2: Reference linear relations and summary statistics of the identified data and data-driven predictions: R^2 values from least-squares regression and relative slope errors with respect to the homogenized parameters. The spread in the polar ratio $(\tau_{21} - \tau_{12})/(\gamma_{21} - \gamma_{12})$ is quantified using the normalized median absolute deviation (NMAD), relative to the reference κ_1 .

Relation	Ref. slope	Identification (DDI)		Prediction (DDCM)	
		Fit	Error [%]	Fit	Error [%]
$(\sigma_{11} + \sigma_{22})/(\varepsilon_{11} + \varepsilon_{22})$	$2(\lambda + \mu)$	$R^2 = 0.99$	2.90	$R^2 = 0.88$	6.55
$\sigma_{12}/\varepsilon_{12}$	2μ	$R^2 = 0.99$	0.73	$R^2 = 0.98$	0.99
$(\tau_{21} - \tau_{12})/(\gamma_{21} - \gamma_{12})$	κ_1	NMAD = 0.76%	0.01	NMAD = 2.05%	0.21

the applied body couple. Therefore, the tight distribution of identified polar ratios $(\tau_{21} - \tau_{12})/(\gamma_{21} - \gamma_{12})$ around the reference κ_1 demonstrates good accuracy. We thus conclude that the identified relations arising from least-squares fitting of the data closely approximate all homogenized material properties.

5.2.2. Data-driven prediction

The identified material data from the honeycomb L-shaped specimen is now used to predict the behavior of a double-notched specimen made of the same material (Figure 7). For this purpose, we employ the micromorphic data-driven simulation framework [45] (section 3), providing an assessment of the reliability of the identified material data for enabling model-free predictions within a generalized continuum.

Figure 11 shows the generalized stress fields $\sigma_{ij} + \tau_{ij}$ at $\bar{u}_2 = 0.35$ mm, comparing the *predicted* mechanical states to the reference homogenized model in the double-notched specimen. As for the identified states in the L-shaped specimen, we observe a striking agreement in all four components. This behavior is also observed in Figure 10, where the predicted generalized stress-strain states lie, as expected,

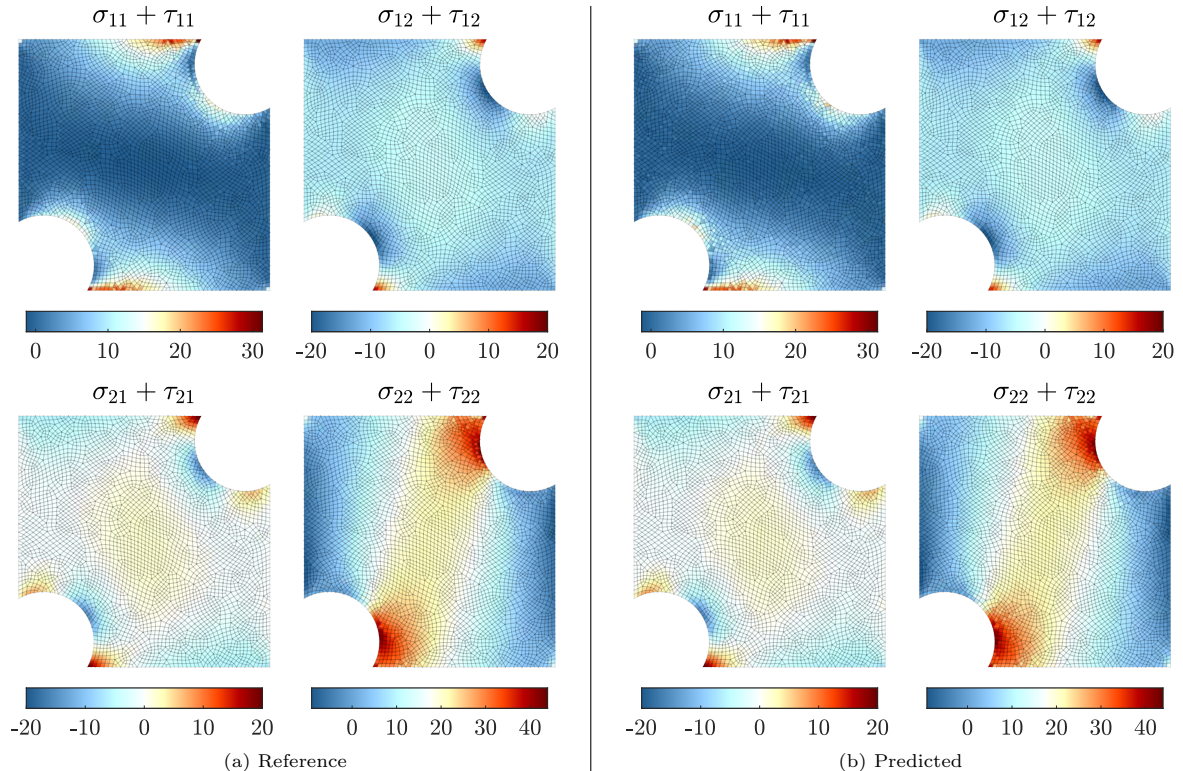


Figure 11: Comparison of generalized stress fields $\sigma_{ij} + \tau_{ij}$ [kPa] in the honeycomb double-notched specimen, showing (a) the ground-truth homogenized model simulation and (b) the *predicted* mechanical stress fields.

Table 3: Metric distances of the phase-space coordinates $\mathbf{z} = (\boldsymbol{\varepsilon}, \boldsymbol{\gamma}, \boldsymbol{\sigma}, \boldsymbol{\tau})$ in the honeycomb double-notched specimen: relative errors of the data-driven simulation (DDCM) and relative errors with respect to the reference homogenized model.

Variable	Metric $d(\cdot)$	DDCM, $100 \frac{d(\square - \bar{\square})}{d(\square)} [\%]$	Reference, $100 \frac{d(\square - \square_{\text{ref}})}{d(\square_{\text{ref}})} [\%]$
Strain $\boldsymbol{\varepsilon}$	$\ \cdot\ _{\mathbf{C}}$	6.35	4.10
Stress $\boldsymbol{\sigma}$	$\ \cdot\ _{\mathbf{C}^{-1}}$	5.88	6.81
Rel. strain $\boldsymbol{\gamma}$	$\ \cdot\ _{\mathbf{D}}$	4.06	1.81
Rel. stress $\boldsymbol{\tau}$	$\ \cdot\ _{\mathbf{D}^{-1}}$	0.69	3.76
All \mathbf{z}	$\ \cdot\ $	5.61	5.19

within the DDI data points and are closely distributed around the reference response. In particular, the tendency towards the expected linear relations is confirmed by the statistics in Table 2. Furthermore, Figure 12 presents the kinematic fields (u_1, u_2, θ_3), comparing the direct numerical simulation of the discrete metastructure to the homogenized model and the data-driven predictions. Again, we observe a notable agreement between the DDI-informed data-driven simulation and the expected response.

The predictive accuracy is further assessed quantitatively in Table 3. Specifically, we report the global

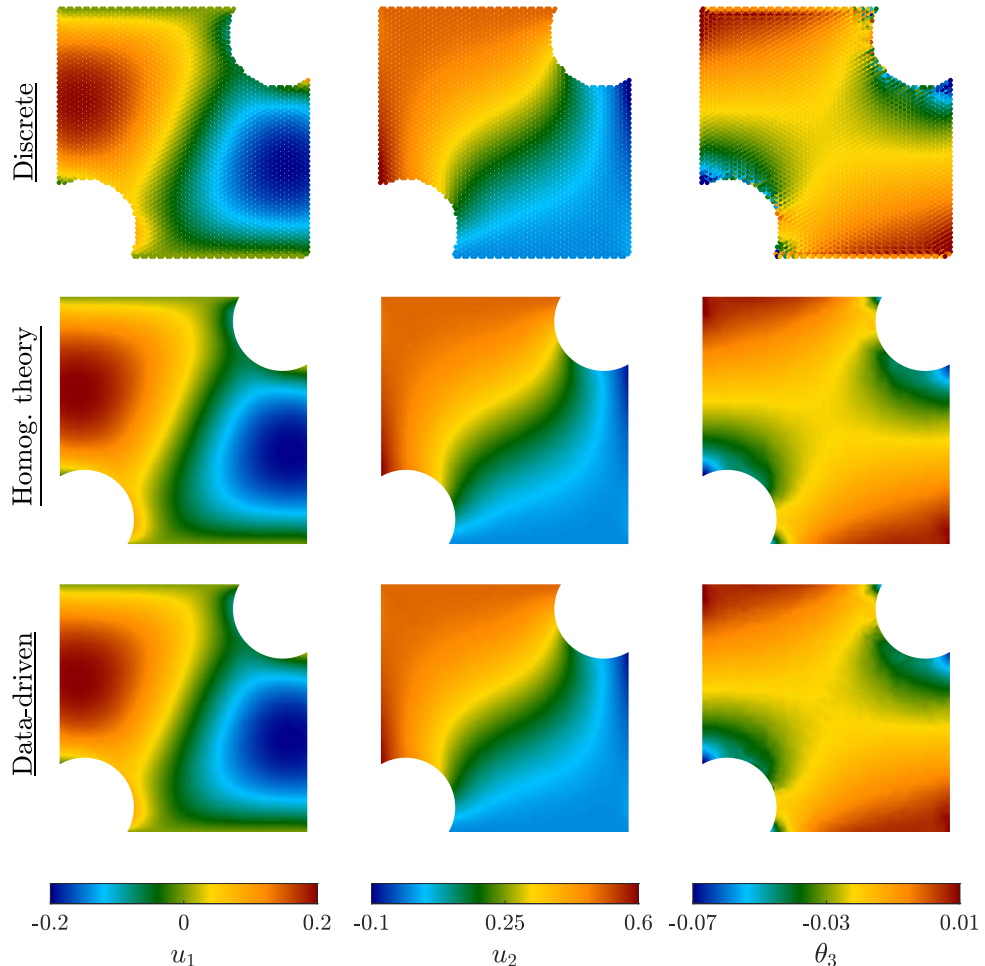


Figure 12: Kinematic fields in the honeycomb double-notched specimen: displacements u_i [mm] and microrotations θ_3 , showing the direct numerical simulation of the discrete metastructure (top), the homogenized model (middle), and the DDI-informed data-driven predictions (bottom).

distance metric (14) and its individual contributions from each phase-space variable, namely

$$\|\mathbf{z}\|^2 = \underbrace{\frac{1}{2} \sum_{e=1}^M w_e \mathbf{C}_e \boldsymbol{\varepsilon}_e \cdot \boldsymbol{\varepsilon}_e}_{\|\boldsymbol{\varepsilon}\|_{\mathbf{C}}^2} + \underbrace{\frac{1}{2} \sum_{e=1}^M w_e \mathbf{C}_e^{-1} \boldsymbol{\sigma}_e \cdot \boldsymbol{\sigma}_e}_{\|\boldsymbol{\sigma}\|_{\mathbf{C}^{-1}}^2} + \underbrace{\frac{1}{2} \sum_{e=1}^M w_e \mathbf{D}_e \boldsymbol{\gamma}_e \cdot \boldsymbol{\gamma}_e}_{\|\boldsymbol{\gamma}\|_{\mathbf{D}}^2} + \underbrace{\frac{1}{2} \sum_{e=1}^M w_e \mathbf{D}_e^{-1} \boldsymbol{\tau}_e \cdot \boldsymbol{\tau}_e}_{\|\boldsymbol{\tau}\|_{\mathbf{D}^{-1}}^2},$$

considering (i) the errors between the predicted material solution $\bar{\mathbf{z}}$ and the mechanical solution \mathbf{z} , and (ii) the errors between the predicted mechanical solution \mathbf{z} and the reference homogenized solution \mathbf{z}_{ref} . All error metrics remain well below 10%, confirming the reliability of the identified data for predicting the response of unseen BVPs in a generalized continuum.

6. Summary and concluding remarks

We have presented a data-driven identification (DDI) framework to obtain material data from full-field kinematics and force measurements in generalized continua. The framework is formulated within the general setting of micromorphic materials at small strains. By adopting a model-free data-driven approach, we have relied on (i) non-classical compatibility and balance equations, and (ii) availability of full-field kinematic data—displacements and microdeformations—and the corresponding applied forces to identify the associated generalized stress fields along with a representative material dataset. Notably, our approach circumvents the definition of heuristic kinematics and boundary conditions typically required in RVE-based micromorphic homogenization methods. The identified data is suitable for either calibration of constitutive models or model-free data-driven simulations of generalized continua.

The reliability of the identification process was first validated via synthetic studies on a sample with geometrical defects, assuming material behavior governed by a full first-order micromorphic model. We then presented an application to mechanical metamaterials, including predictions in unseen boundary value problems. In this case, the ground-truth behavior used for benchmarking is available from homogenization theory and corresponds to a zeroth-order micropolar continuum. In all cases, excellent agreement was observed between the identified generalized stress-strain states and the reference response, including non-trivial features such as non-symmetric and third-order stress components.

Future studies may include applications to elastoplastic or other non-linear composites at small strains, which, in principle, are not excluded by the present framework as long as the material behavior remains stable. Extensions to account for material instabilities as well as finite deformations remain open challenges. We further emphasize that the present approach remains agnostic with respect to the constitutive model, while the general kinematic ansatz inherent to micromorphic media is assumed as a point of departure. This approach is sufficiently general to encompass a wide range of continuum behaviors as special cases, including continuum limits with provable convergence from discrete systems (e.g., the example in section 5.2). Ultimately, the specific form of the continuum should be established through such rigorous homogenization analyses, which may reveal the relevant phase-space quantities without necessarily yielding explicit, closed-form parameters. In those scenarios, the present data-driven framework provides a flexible means of identifying material data that may otherwise not be directly accessible.

Acknowledgements

JU gratefully acknowledges support from the Digital Twins seed funding initiative provided by the Department of Mechanical Engineering at the University of Michigan. LS gratefully acknowledges the

financial support of Nantes Université excellence program NExT, through the funding of International Research Partnership project iDDrEAM.

Appendix A. Metric tensors

Let us recall that, in the local distance metric (13), the phase-space coordinates

$$(\boldsymbol{\varepsilon}_e, \boldsymbol{\sigma}_e) \in \mathbb{R}^{n_\varepsilon} \times \mathbb{R}^{n_\varepsilon}, \quad (\boldsymbol{\gamma}_e, \boldsymbol{\tau}_e) \in \mathbb{R}^{n_\chi} \times \mathbb{R}^{n_\chi}, \quad (\boldsymbol{\zeta}_e, \boldsymbol{\mu}_e) \in \mathbb{R}^{n_\zeta} \times \mathbb{R}^{n_\zeta}$$

are Voigt representations of the generalized stress-strain states

$$(\boldsymbol{\varepsilon}, \boldsymbol{\sigma}) \in \mathbb{R}_{\text{sym}}^{n \times n} \times \mathbb{R}_{\text{sym}}^{n \times n}, \quad (\boldsymbol{\gamma}, \boldsymbol{\tau}) \in \mathbb{R}^{n \times n} \times \mathbb{R}^{n \times n}, \quad (\boldsymbol{\zeta}, \boldsymbol{\mu}) \in \mathbb{R}^{n \times n \times n} \times \mathbb{R}^{n \times n \times n}.$$

Hence, the metric tensors $\mathbf{C}_e \in \mathbb{R}_{\text{sym},+}^{n_\varepsilon \times n_\varepsilon}$, $\mathbf{D}_e \in \mathbb{R}_{\text{sym},+}^{n_\chi \times n_\chi}$, and $\mathbf{A}_e \in \mathbb{R}_{\text{sym},+}^{n_\zeta \times n_\zeta}$ also correspond to Voigt representations of tensors \mathbf{C} (fourth-order), \mathbf{D} (fourth-order), and \mathbf{A} (sixth-order).

In standard isotropic constitutive models, \mathbf{C} owns the usual minor and major symmetries $C_{ijkl} = C_{jilk} = C_{klij}$, while, owing to the non-symmetry of $\boldsymbol{\chi}$, in general, \mathbf{D} and \mathbf{A} only possess major symmetries $D_{ijkl} = D_{klji}$ and $A_{ijklmn} = A_{lmnijk}$. However, the data-driven approach treats these as numerical operators. As such, we choose simple forms with the following structure:

$$C_{ijkl} = \lambda \delta_{ij} \delta_{kl} + \mu (\delta_{ik} \delta_{jl} + \delta_{il} \delta_{jk}), \quad (\text{A.1})$$

$$D_{ijkl} = c_1 C_{ijkl} + \kappa_1 (\delta_{ik} \delta_{jl} - \delta_{il} \delta_{jk}), \quad (\text{A.2})$$

$$A_{ijklmn} = \ell^2 C_{ijlm} \delta_{kn} + \mu \ell^2 (\delta_{il} \delta_{jm} - \delta_{im} \delta_{jl}) \delta_{kn}. \quad (\text{A.3})$$

The generalized phase space is then metrized by five non-negative metric constants, $\boldsymbol{\theta} := (\lambda, \mu, c_1, \kappa_1, \ell)$.

A convenient strategy to define these coefficients objectively, adopted in Karapiperis et al. [43] for micropolar continua, is to minimize the distance (13), locally or globally, at fixed mechanical and material states $(\mathbf{z}_e, \bar{\mathbf{z}}_e)$ but varying metric constants. For instance, for the global case,

$$\boldsymbol{\theta} \in \arg \min_{\tilde{\boldsymbol{\theta}} \in \mathbb{R}_+^5} \|\bar{\mathbf{z}} - \mathbf{z}\|^2(\tilde{\boldsymbol{\theta}}), \quad (\text{A.4})$$

where we write the dependence of the global distance metric on the metric constants explicitly. This procedure is not employed here for the sake of simplicity but can be incorporated in Algorithm 1 to ensure optimal metric tensors (A.3) free of any modeling bias.

References

- [1] G.A. Maugin. Generalized continuum mechanics: what do we mean by that? In *Mechanics of Generalized Continua: One hundred years after the Cosserats*, pages 3–13. Springer, 2010.
- [2] E.M.P. Cosserat and F. Cosserat. *Théorie des corps déformables*. A. Hermann et fils, 1909.
- [3] S. Forest and R. Sievert. Nonlinear microstrain theories. *International Journal of Solids and Structures*, 43(24):7224–7245, 2006.
- [4] N. Triantafyllidis and E.C. Aifantis. A gradient approach to localization of deformation. I. Hyperelastic materials. *Journal of Elasticity*, 16(3):225–237, 1986.

[5] M. Lazar, G.A. Maugin, and E.C. Aifantis. On a theory of nonlocal elasticity of bi-Helmholtz type and some applications. *International Journal of Solids and Structures*, 43(6):1404–1421, 2006.

[6] A.C. Eringen. Mechanics of micromorphic continua. In *Mechanics of generalized continua: proceedings of the IUTAM-Symposium on the Generalized Cosserat Continuum and the Continuum Theory of Dislocations with Applications, Freudenstadt and Stuttgart (Germany) 1967*, pages 18–35. Springer, 1968.

[7] M.P. Ariza, S. Conti, and M. Ortiz. Homogenization and continuum limit of mechanical metamaterials. *Mechanics of Materials*, 196:105073, 2024.

[8] R.N. Glaesener, C. Lestringant, B. Telgen, and D.M. Kochmann. Continuum models for stretching-and bending-dominated periodic trusses undergoing finite deformations. *International Journal of Solids and Structures*, 171:117–134, 2019.

[9] H. Xu, I. Tobasco, and P. Plucinsky. Derivation of an effective plate theory for parallelogram origami from bar and hinge elasticity. *Journal of the Mechanics and Physics of Solids*, 192:105832, 2024.

[10] M. Sarhil, L. Scheunemann, P. Lewintan, J. Schröder, and P. Neff. A computational approach to identify the material parameters of the relaxed micromorphic model. *Computer Methods in Applied Mechanics and Engineering*, 425:116944, 2024.

[11] H.-B. Mühlhaus and E.C. Aifantis. A variational principle for gradient plasticity. *International Journal of Solids and Structures*, 28(7):845–857, 1991.

[12] S. Forest and E. Lorentz. Localization phenomena and regularization methods. *Local Approach to Fracture*, 1:311–371, 2004.

[13] N.A. Collins-Craft, I. Stefanou, J. Sulem, and I. Einav. A Cosserat Breakage Mechanics model for brittle granular media. *Journal of the Mechanics and Physics of Solids*, 141:103975, 2020.

[14] J.Y. Chen, Y. Huang, and M. Ortiz. Fracture analysis of cellular materials: a strain gradient model. *Journal of the Mechanics and Physics of Solids*, 46(5):789–828, 1998.

[15] T. Dillard, S. Forest, and P. Ienny. Micromorphic continuum modelling of the deformation and fracture behaviour of nickel foams. *European Journal of Mechanics-A/Solids*, 25(3):526–549, 2006.

[16] M.B. Rubin and L. Bardella. An Eulerian thermodynamical formulation of size-dependent plasticity. *Journal of the Mechanics and Physics of Solids*, 170:105122, 2023.

[17] J. Ulloa, M.P. Ariza, J.E. Andrade, and M. Ortiz. Fracture and size effect in mechanical metamaterials. *Journal of the Mechanics and Physics of Solids*, 193:105860, 2024.

[18] A. Madeo, P. Neff, I.D. Ghiba, L. Placidi, and G. Rosi. Wave propagation in relaxed micromorphic continua: modeling metamaterials with frequency band-gaps. *Continuum Mechanics and Thermodynamics*, 27:551–570, 2015.

[19] A. Misra and P. Poorsolhjouy. Granular micromechanics based micromorphic model predicts frequency band gaps. *Continuum Mechanics and Thermodynamics*, 28:215–234, 2016.

[20] K. Dayal. Leading-order nonlocal kinetic energy in peridynamics for consistent energetics and wave dispersion. *Journal of the Mechanics and Physics of Solids*, 105:235–253, 2017.

[21] M. Shaat. A reduced micromorphic model for multiscale materials and its applications in wave propagation. *Composite Structures*, 201:446–454, 2018.

[22] E.A. Ivanova. On a new theory of the Cosserat continuum with applications in electrodynamics. In *Recent Approaches in the Theory of Plates and Plate-Like Structures*, pages 75–87. Springer, 2021.

[23] A.C. Eringen and E.S. Suhubi. Nonlinear theory of simple micro-elastic solids—I. *International Journal of Engineering Science*, 2(2):189–203, 1964.

[24] A.C. Eringen. *Microcontinuum field theories: I. Foundations and solids*. Springer Science & Business Media, 2012.

[25] R.D. Mindlin. Microstructures in linear elasticity. *Archives for Rational Mechanics and Analysis*, 16:51–78, 1964.

[26] P. Germain. The method of virtual power in continuum mechanics. Part 2: Microstructure. *SIAM Journal on Applied Mathematics*, 25(3):556–575, 1973.

[27] P. Neff, I.D. Ghiba, A. Madeo, L. Placidi, and G. Rosi. A unifying perspective: the relaxed linear micromorphic continuum. *Continuum Mechanics and Thermodynamics*, 26:639–681, 2014.

[28] S. Forest and R. Sievert. Elastoviscoplastic constitutive frameworks for generalized continua. *Acta Mechanica*, 160(1):71–111, 2003.

[29] R.A. Regueiro. Finite strain micromorphic pressure-sensitive plasticity. *Journal of Engineering Mechanics*, 135(3):178–191, 2009.

[30] E.C. Bryant and W. Sun. A micromorphically regularized Cam-clay model for capturing size-dependent anisotropy of geomaterials. *Computer Methods in Applied Mechanics and Engineering*, 354:56–95, 2019.

[31] M. Rys, S. Forest, and H. Petryk. A micromorphic crystal plasticity model with the gradient-enhanced incremental hardening law. *International Journal of Plasticity*, 128:102655, 2020.

[32] M. Lindroos, J.-M. Scherer, S. Forest, A. Laukkanen, T. Andersson, J. Vaara, A. Mäntylä, and T. Frondelius. Micromorphic crystal plasticity approach to damage regularization and size effects in martensitic steels. *International Journal of Plasticity*, 151:103187, 2022.

[33] O. Aslan, N.M. Cordero, A. Gaubert, and S. Forest. Micromorphic approach to single crystal plasticity and damage. *International Journal of Engineering Science*, 49(12):1311–1325, 2011.

[34] C. Miehe, F. Aldakheel, and S. Teichtmeister. Phase-field modeling of ductile fracture at finite strains: A robust variational-based numerical implementation of a gradient-extended theory by micromorphic regularization. *International Journal for Numerical Methods in Engineering*, 111(9):816–863, 2017.

[35] T. Brepols, S. Wulffinghoff, and S. Reese. Gradient-extended two-surface damage-plasticity: micromorphic formulation and numerical aspects. *International Journal of Plasticity*, 97:64–106, 2017.

[36] B. Yin, D. Zhao, J. Storm, and M. Kaliske. A micromorphic damage model based on a gradient extension for robust crack deformations. *Computer Methods in Applied Mechanics and Engineering*, 399:115328, 2022.

[37] S. Forest. Micromorphic approach for gradient elasticity, viscoplasticity, and damage. *Journal of Engineering Mechanics*, 135(3):117–131, 2009.

[38] T. Kirchdoerfer and M. Ortiz. Data-driven computational mechanics. *Computer Methods in Applied Mechanics and Engineering*, 304:81–101, 2016.

[39] R. Eggersmann, T. Kirchdoerfer, S. Reese, L. Stainier, and M. Ortiz. Model-free data-driven inelasticity. *Computer Methods in Applied Mechanics and Engineering*, 350:81–99, 2019.

[40] K. Karapiperis, L. Stainier, M. Ortiz, and J.E. Andrade. Data-driven multiscale modeling in mechanics. *Journal of the Mechanics and Physics of Solids*, 147:104239, 2021.

[41] J. Ulloa, A. Gorgogianni, K. Karapiperis, M. Ortiz, and J.E. Andrade. Data-driven breakage mechanics: Predicting the evolution of particle-size distribution in granular media. *Journal of the Mechanics and Physics of Solids*, 178:105328, 2023.

[42] E. Prume, C. Gierden, M. Ortiz, and S. Reese. Direct data-driven algorithms for multiscale mechanics. *Computer Methods in Applied Mechanics and Engineering*, 433:117525, 2025.

[43] K. Karapiperis, M. Ortiz, and J.E. Andrade. Data-Driven nonlocal mechanics: Discovering the internal length scales of materials. *Computer Methods in Applied Mechanics and Engineering*, 386:114039, 2021.

[44] V. Kamasamudram and L. Stainier. A strain based Lipschitz regularization for materials undergoing damage. *Comptes Rendus. Mécanique*, 351(G1):125–149, 2023.

[45] J. Ulloa, L.S., M. Ortiz, and J.E. Andrade. Data-driven micromorphic mechanics for materials with strain localization. *Computer Methods in Applied Mechanics and Engineering*, 429:117180, 2024.

[46] A. Misra and P. Poorsolhjouy. Identification of higher-order elastic constants for grain assemblies based upon granular micromechanics. *Mathematics and Mechanics of Complex Systems*, 3(3):285–308, 2015.

[47] S. Forest and K. Sab. Cosserat overall modeling of heterogeneous materials. *Mechanics Research Communications*, 25(4):449–454, 1998.

[48] F. Feyel. A multilevel finite element method (FE2) to describe the response of highly non-linear structures using generalized continua. *Computer Methods in applied Mechanics and engineering*, 192(28-30):3233–3244, 2003.

[49] M.L. De Bellis and D. Addessi. A Cosserat based multi-scale model for masonry structures. *International Journal for Multiscale Computational Engineering*, 9(5), 2011.

[50] V.G. Kouznetsova, M.G.D. Geers, and W.A.M. Brekelmans. Multi-scale constitutive modelling of heterogeneous materials with a gradient-enhanced computational homogenization scheme. *International Journal for Numerical Methods in Engineering*, 54(8):1235–1260, 2002.

[51] V.G. Kouznetsova, M.G.D. Geers, and W.A.M. Brekelmans. Multi-scale second-order computational homogenization of multi-phase materials: a nested finite element solution strategy. *Computer Methods in Applied Mechanics and Engineering*, 193(48-51):5525–5550, 2004.

[52] V.-D. Nguyen, G. Becker, and L. Noels. Multiscale computational homogenization methods with a gradient enhanced scheme based on the discontinuous galerkin formulation. *Computer Methods in Applied Mechanics and Engineering*, 260:63–77, 2013.

[53] S. Forest. Homogenization methods and mechanics of generalized continua-part 2. *Theoretical and Applied Mechanics*, (28-29):113–144, 2002.

[54] R. Jänicke and H. Steeb. Minimal loading conditions for higher-order numerical homogenisation schemes: Cauchy, second gradient and micromorphic substitute media. *Archive of Applied Mechanics*, 82:1075–1088, 2012.

[55] S.E. Alavi, J.-F. Ganghoffer, H. Reda, and M. Sadighi. Construction of micromorphic continua by homogenization based on variational principles. *Journal of the Mechanics and Physics of Solids*, 153:104278, 2021.

[56] R. Biswas and L.H. Poh. A micromorphic computational homogenization framework for heterogeneous materials. *Journal of the Mechanics and Physics of Solids*, 102:187–208, 2017.

[57] W. Ehlers and S. Bidier. From particle mechanics to micromorphic media. Part I: Homogenisation of discrete interactions towards stress quantities. *International Journal of Solids and Structures*, 187:23–37, 2020.

[58] O. Rokoš, M.M. Ameen, R.H.J. Peerlings, and M.G.D. Geers. Micromorphic computational homogenization for mechanical metamaterials with patterning fluctuation fields. *Journal of the Mechanics and Physics of Solids*, 123:119–137, 2019.

[59] P. Neff, B. Eidel, M.V. d’Agostino, and A. Madeo. Identification of scale-independent material parameters in the relaxed micromorphic model through model-adapted first order homogenization. *Journal of Elasticity*, 139(2):269–298, 2020.

[60] N.A. Miller, R.A. Regueiro, F. Shahabi, and J.E. Bishop. A micromorphic filter for determining stress and deformation measures from direct numerical simulations of lower length scale behavior. *International Journal for Numerical Methods in Engineering*, 123(17):3879–3921, 2022.

[61] A. Leygue, M. Coret, J. Réthoré, L. Stainier, and E. Verron. Data-based derivation of material response. *Computer Methods in Applied Mechanics and Engineering*, 331:184–196, 2018.

[62] L. Stainier, A. Leygue, and M. Ortiz. Model-free data-driven methods in mechanics: material data identification and solvers. *Computational Mechanics*, 64(2):381–393, 2019.

[63] S. Forest and D.K. Trinh. Generalized continua and non-homogeneous boundary conditions in homogenisation methods. *ZAMM-Journal of Applied Mathematics and Mechanics/Zeitschrift für Angewandte Mathematik und Mechanik*, 91(2):90–109, 2011.

[64] G. Hütter. A theory for the homogenisation towards micromorphic media and its application to size effects and damage, 2019. Habilitation Thesis. ISBN: 978-2-86012-603-5, <http://nbn-resolving.de/urn:nbn:de:bsz:105-qucosa2-331790>.

[65] N. Hachem, A. Leygue, and L. Stainier. Mathematical and numerical assessment of data-driven identification method applied to nonlinear elasticity. *Computer Methods in Applied Mechanics and Engineering*, 446:118273, 2025.

[66] A. Leygue. On the formulation and convergence of Data-Driven Identification. *Comptes Rendus Mécanique*, 353:761–773, 2025.

[67] M.P. Ariza, S. Conti, and M. Ortiz. Homogenization and continuum limit of mechanical metamaterials. *Mechanics of Materials*, 196:105073, 2024.

[68] J. Ulloa, M.P. Ariza, J.E. Andrade, and M. Ortiz. Homogenized models of mechanical metamaterials. *Computer Methods in Applied Mechanics and Engineering*, 433:117454, 2025.